Ore Geology Reviews 90 (2017) 36–51

Contents lists available at ScienceDirect

Ore Geology Reviews

journal homepage: www.elsevier.com/locate/oregeorev

Isotope geochemistry and geochronology of the Niujuan silver deposit, northern North China Craton: Implications for magmatism and metallogeny in an extensional tectonic setting

Yu-Jie Li[a,b], Sheng-Rong Li[a,b,*], M. Santosh[b,c], Xuan-Xue Mo[b], Kai-Bo Gao[a,b], Yuan Ma[a,b]

[a] State Key Laboratory of Geological Processes and Mineral Resources, China University of Geosciences, Beijing 100083, China
[b] School of Earth Science and Resources, China University of Geosciences, Xueyuan Road, Haidian District, Beijing 100083, China
[c] Department of Earth Sciences, University of Adelaide, Adelaide, SA 5005, Australia

ARTICLE INFO

Keywords:
Zircon U-Pb geochronology
Stable isotopes
Fluorite Sm–Nd geochronology
Niujuan silver deposit
Northern North China Craton

ABSTRACT

The Niujuan breccia-type silver deposit forms part of the North Hebei metallogenic belt along the northern margin of the North China Craton. The Hercynian Baiyingou coarse-grained granite and the Yanshanian Er'daogou fine-grained granite are the major Mesozoic intrusions exposed in this region. Here we investigate the salient characteristics of the mineralization and evaluate its genesis through zircon U-Pb and fluorite Sm-Nd age data, and Pb, S, O, H, He and Ar isotope data. The orebodies of the Niujuan silver deposit are hosted in breccias, which contain angular fragments of the Baiyingou and Er'daogou granitoids. The $\delta^{34}S$ values of pyrite from the silver mineralized veins range from 2.4‰ to 5.3‰. The $^{206}Pb/^{204}Pb$, $^{207}Pb/^{204}Pb$ and $^{208}Pb/^{204}Pb$ ratios of the sulfide minerals show ranges of 16.837–16.932, 15.420–15.501 and 37.599–37.950, respectively. The $^{3}He/^{4}He$ and $^{40}Ar/^{36}Ar$ ratios of the fluids trapped in pyrite are 0.921–4.81Ra and 299.34–303.84, respectively. The $\delta^{18}O$ and $\delta^{18}D_w$ values of the ore-forming fluids range from 0.6‰ to −4.15‰ and from −119.4‰ to −98.7‰, respectively. Our isotopic data suggest that the ore-forming fluids were originally derived from the subvolcanic plutons and evolved into a mixture of magmatic and meteoric water during the main hydrothermal stage. The ore-forming materials were primarily derived from the lower crust with limited incorporation of mantle materials. The emplacement time of the Er'daogou granite is constrained by LA-ICP-MS zircon U-Pb geochronology at 145.5 ± 2.1 Ma. Five fluorite samples from the last hydrothermal stage yielded a Sm-Nd isochron age of 139.2 ± 3.8 Ma, indicating the upper age limit for the silver mineralization. These ages correlate with the formation of the Niujuan deposit in an extensional setting associated with the closure of the Mongol-Okhotsk Ocean and the subduction of the Paleo-Pacific oceanic plate beneath the North China Craton.

1. Introduction

The Circum Pacific metallogenic domain is one of the main regions for global silver resources. Since the 1970s, a large number of continental volcanic rock-hosted silver deposits were discovered in the eastern and southwestern parts of this metallogenic domain (mainly in the U.S., Canada, Mexico, Bolivia and Australia) (Smith et al., 1982; Cunningham et al., 1991; Mango et al., 1991; Musgrave and Thompson, 1991; Babcock et al., 1995; Liu and Zhang, 1997; Long et al., 1998). Subsequent studies led to the identification of a silver polymetallic metallogenic belt in North Hebei within the northern part of the North China Craton (NCC) (Fig. 1). This belt has now become an important silver province in China. It is believed that the complex tectonic processes associated with cratonization and craton destruction of the NCC and the related multiple magmatic activities in this region provided favorable conditions for metallogenesis (Zhu et al., 2012; Zhang et al., 2013; Li et al., 2014; Li and Santosh, 2014). The classification, metallogenesis and prospecting criteria of silver deposits in this region were the focus of several investigations in the past (Li and Geng, 1997; Wang et al., 2005; Yang and Lv, 2006; Zhang and Zhao, 2009; Li and Santosh, 2014). The continental volcanic rock-hosted silver deposits in the North Hebei metallogenic belt can be further divided into two types: (1) continental volcano-magmatic hydrothermal silver deposits which are mainly distributed in the regions with intense late Jurassic to early Cretaceous volcanic activities (such as the Xiangguang, Pengjiagou, and Xiaokouhuaying deposits), and (2) continental subvolcano-magmatic hydrothermal silver deposits which are related to the more widely distributed Yanshanian subvolcanic granitoids (such as the Caijiaying,

* Corresponding author at: State Key Laboratory of Geological Processes and Mineral Resources, China University of Geosciences, Beijing 100083, China.
E-mail address: lisr@cugb.edu.cn (S.-R. Li).

http://dx.doi.org/10.1016/j.oregeorev.2017.10.004
Received 17 March 2017; Received in revised form 4 October 2017; Accepted 5 October 2017
Available online 12 October 2017
0169-1368/

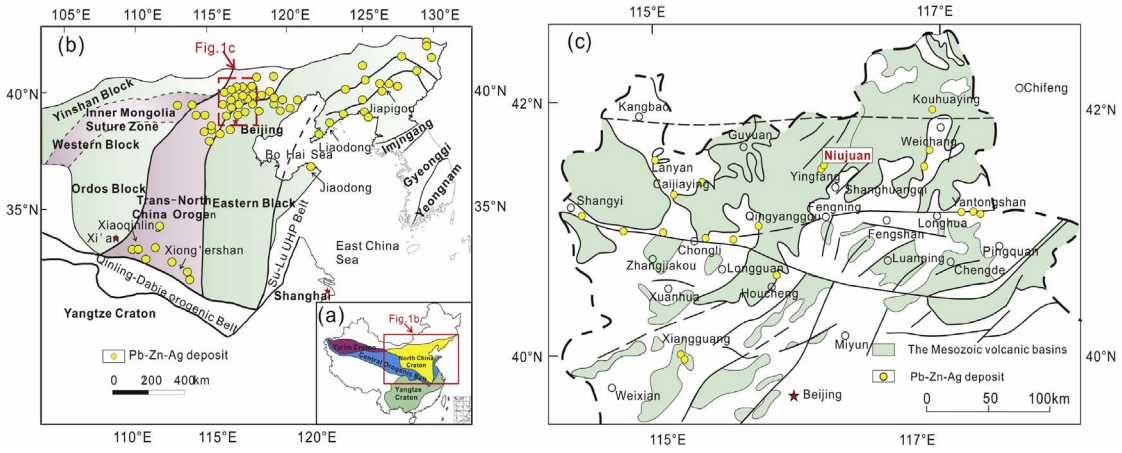

Fig. 1. (a) Simplified tectonic map of China showing the major cratons (after Zhao et al., 2000). (b) Sketch map of the NCC showing the distribution of silver-polymetallic deposits (after Santosh et al., 2010; Li et al., 2013). (c) Regional geological map of the North Hebei showing the distribution of silver-polymetallic deposits (after Yang, 2000).

Shuiguankou, Wanquansi, and Guzigou deposits) (Fig. 1c).

The Niujuan silver deposit, discovered in the 1990s, is one of the important deposits in the North Hebei polymetallic belt and occurs along the NNE-trending Shanghuangqi tectonomagmatic belt (Li, 2006; Yang, 2000; Li et al., 2011). The deposit has an estimated silver reserve of 652 tonnes with an average grade of 277.85 g/t. Detailed studies on this deposit are important in understanding the tectonic setting and genesis of continental volcanic rock-hosted silver deposits, which in turn would aid formulating exploration strategies for the silver-polymetallic deposits in North Hebei.

In this study, we document the geological characteristics of the Niujuan silver deposit, including the structural framework, ore petrology, wall rock alteration and nature of mineralization. We also report zircon U-Pb and Sm-Nd isotopic ages, as well as stable isotope (S, Pb, H and O) and noble gas isotope (He and Ar) data. Our study constrains the timing of the ore mineralization, the source of the ore-forming fluid and metals, and the mechanism of mineralization. The results are employed to evaluate the geodynamic background of silver deposits in the northern part of the NCC.

2. Regional geology

The cratonization of the NCC started at the end of Neoarchean (Zhao, 1993; Li et al., 2000; Zhai, 2004) and is considered to have involved the assembly of several Archean micro-continents (Zhai and Santosh, 2011; Yang et al., 2016; Santosh et al., 2016; Yang and Santosh, 2017). During the Paleoproterozoic (1950–1700 Ma), the NCC was involved in a collision of large continental blocks and final cratonization accompanied by long-lived arc magmatism culminating in high- and ultrahigh temperature metamorphism (e.g., Santosh, 2010; Zhao and Zhai, 2013; Yang and Santosh, 2015a). After a prolonged period of quiescence (Zhai, 2010), the NCC was involved in a major tectonic transition during the Mesozoic with extensive erosion of the cratonic root and lithospheric thinning associated with the transition from a compressional to an extensional setting (Xu et al., 2004). During the Triassic to the Cretaceous, the NCC underwent intracontinental extension with igneous intrusions and volcanic eruptions, which were also associated with the formation of major ore belts including the North Hebei silver polymetallic belt (Xu et al., 1995; Kerrich et al., 2000; Sibson, 1994; Heinrich, 2007; Hu et al., 2005; Goldfarb and Santosh, 2014; Li et al., 2015; Groves and Santosh, 2016; Li et al., 2016).

The Niujuan silver deposit in the north-central part of the North Hebei belt is located at the contact zone between the NE-trending Shanghuangqi tectono-magmatic belt and the Datan fault-depression basin in the northern margin of the Inner Mongolian axis (Fig. 1c). The basement rocks are composed of the Paleoproterozoic Hongqiyingzi Group metamorphic rocks, which are covered by the early Mesozoic (Jurassic to Cretaceous) continental facies volcanic rocks. The Hongqiyingzi Group is composed of graphite biotite plagioclase gneiss, garnet biotite plagioclase gneiss, migmatitic gneiss and marble lenses. The early Mesozoic sequence is distributed in the NE-trending volcanic fault basins and consists of andesite, dacite, rhyolite, rhyolitic tuff and tuffaceous conglomerate.

Multiple magmatic events took place in this region during different episodes, leading to the formation of the Archean serpentinised ultramafic-gabbro-granite complexes, Paleoproterozoic anorthosite-gabbro-granite complexes and Mesozoic intermediate-felsic intrusive rocks occurring as batholiths, stocks and dykes (Nie et al., 2007a,b; Li et al., 2014).

In addition to the Niujuan silver deposit, a number of other deposits are also distributed in this region, controlled by the NW-trending fractures formed during Archean to early Proterozoic, and by the Mesozoic magmatic activity and volcanic fault basins, such as the Lanyan and Caijiaying Pb-Zn-Ag deposit, Zhangmajing U-Al deposit, Kouhuaying Mn-Ag deposit, and Yingfang Pb-Zn deposit (Fig. 1c; Song, 1994; Li et al., 2006; Shen et al., 2012).

3. Geology of the Niujuan silver deposit

3.1. Structural framework

The Niujuan silver deposit is controlled by the 8 km long and 10–40 m wide Niujuan-Laohuba fault that strikes N 25–35° with a SE-dip of 50–65° (Fig. 2a). Previous studies identified three major phases of tectonic activity in this region (Fu and Gao, 1998): (1) a compressional stage prior to the silver mineralization, which produced the cryptoexplosive breccias and some regional mylonites; (2) a dextral detachment stage corresponding to the silver mineralization with associated magmatism, cryptoexplosion and ore-forming hydrothermal activity; and (3) a late detachment stage after the silver mineralization.

3.2. Host rocks

The metamorphosed basement rocks in this region mainly belong to the Hongqiyingzi Group, and include biotite plagioclase gneiss and biotite-bearing amphibolite facies gneiss. Among the Mesozoic granitoids in the Niujuan region, the coarse-grained Baiyingou granite of Hercynian age is the largest outcrop. The Yanshanian Er'daogou fine-grained granite is exposed in the eastern and western parts. In addition, some felsic dykes, mainly quartz diorite, and quartz veins are also found.

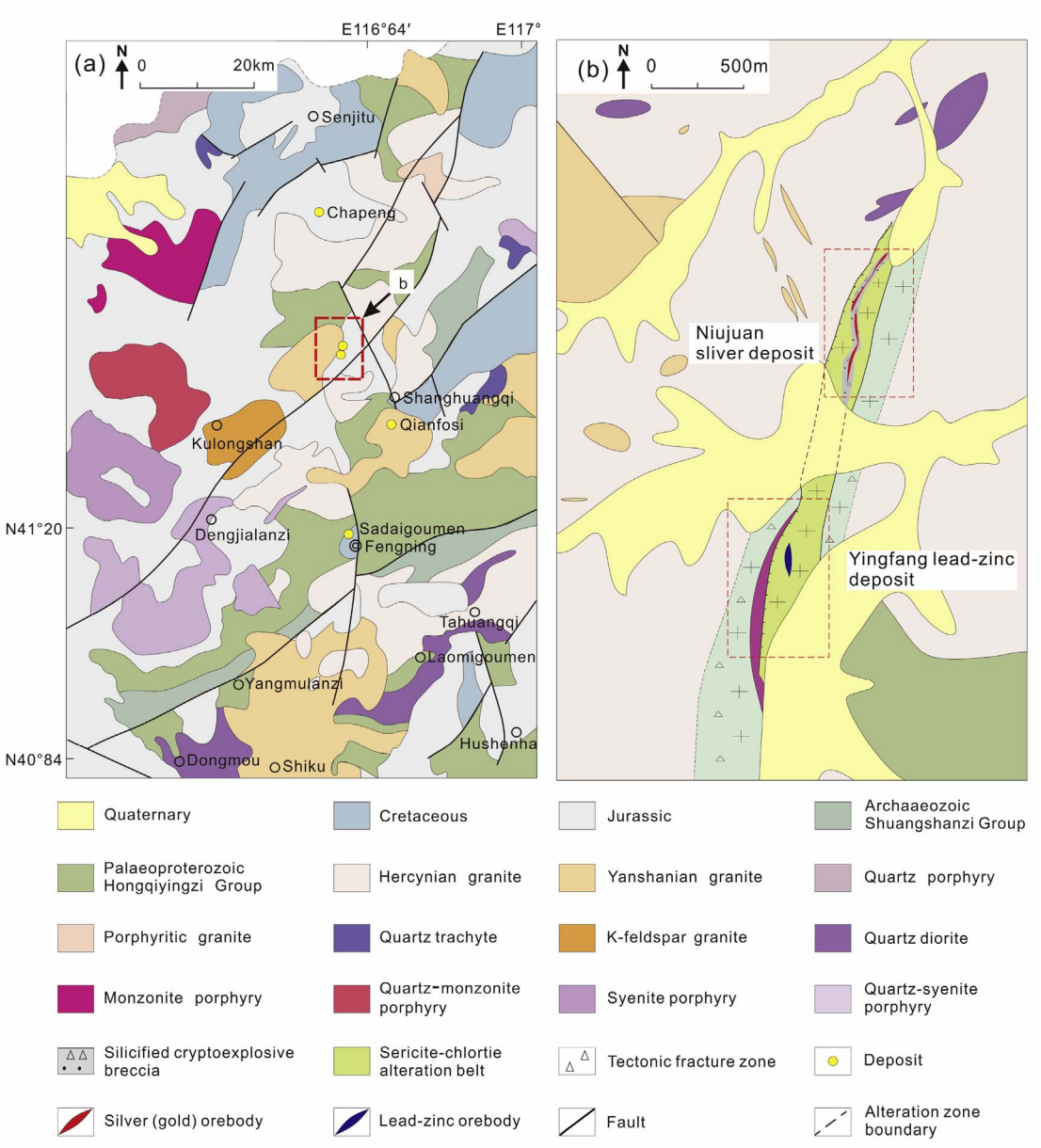

Fig. 2. (a) Regional geological map of the Niujuan silver deposit showing the distribution of magmatic rocks (modified from Shen et al., 2012). (b) Geological map of the Niujuan silver deposit and the Fengning lead-zinc deposit (after Li et al., 2006).

The Niujuan silver deposit, located at the contact zone between the Mesozoic granite and the Hongqiyingzi Group metamorphic rocks, is a breccia-type deposit (Fig. 2b). The breccia belt is about 1 km in length and 40 m in thickness with a NNE-strike and a SE-dip of 50–70°. Five breccia bodies have been identified, extending for more than 650 m in depth. These breccias, in the form of lenses, are controlled by the Niujuan-Laohuba fault.

The breccias are composed of angular fragments of variable size and are compositionally divided into three types: (1) fragments of granite (Fig. 3a, b), tuff (Fig. 3c, d) and silicic breccias (Fig. 3e) with a size range of 2–20 cm; (2) crystal fragments of quartz (Fig. 3f), feldspar, fluorite and pyrite; and (3) fragments formed by the solidification of dacitic magma which is divided into an early stage (M1) and a late stage (M2) representing multiple cryptoexplosions (Fig. 3 g, h). The cement is mainly composed of three types: magmatic, clastic and hydrothermal cement, with the latter two as the dominant types during the mineralization process (Fig. 3).

3.3. Ore bodies

Two orebodies of economic significance are present in the Niujuan silver deposit (Fig. 4a). Orebody I is the largest one, extending NNE for more than 240 m at the surface with a SE-dip. This orebody extends for more than 400 m in depth with thicknesses ranging from 2 to 20 m (Fig. 4b) and with silver grades of 160–750 g/t (average at 527 g/t). Orebody II is parallel to Orebody I and is about 165 m in length at the surface and 2–6 m in thickness, with silver grades ranging from 125 to 810 g/t (averaging at 610 g/t). Orebody II is connected with Orebody I at a depth of about 40–50 m and the joint orebody extends to a depth of more than 450 m.

3.4. Ore mineralogy

In the ores from the Niujuan silver deposit, the metallic minerals are mainly pyrite, galena, sphalerite, argentite and native silver, with minor chalcopyrite, molybdenite, hematite, limonite and electrum

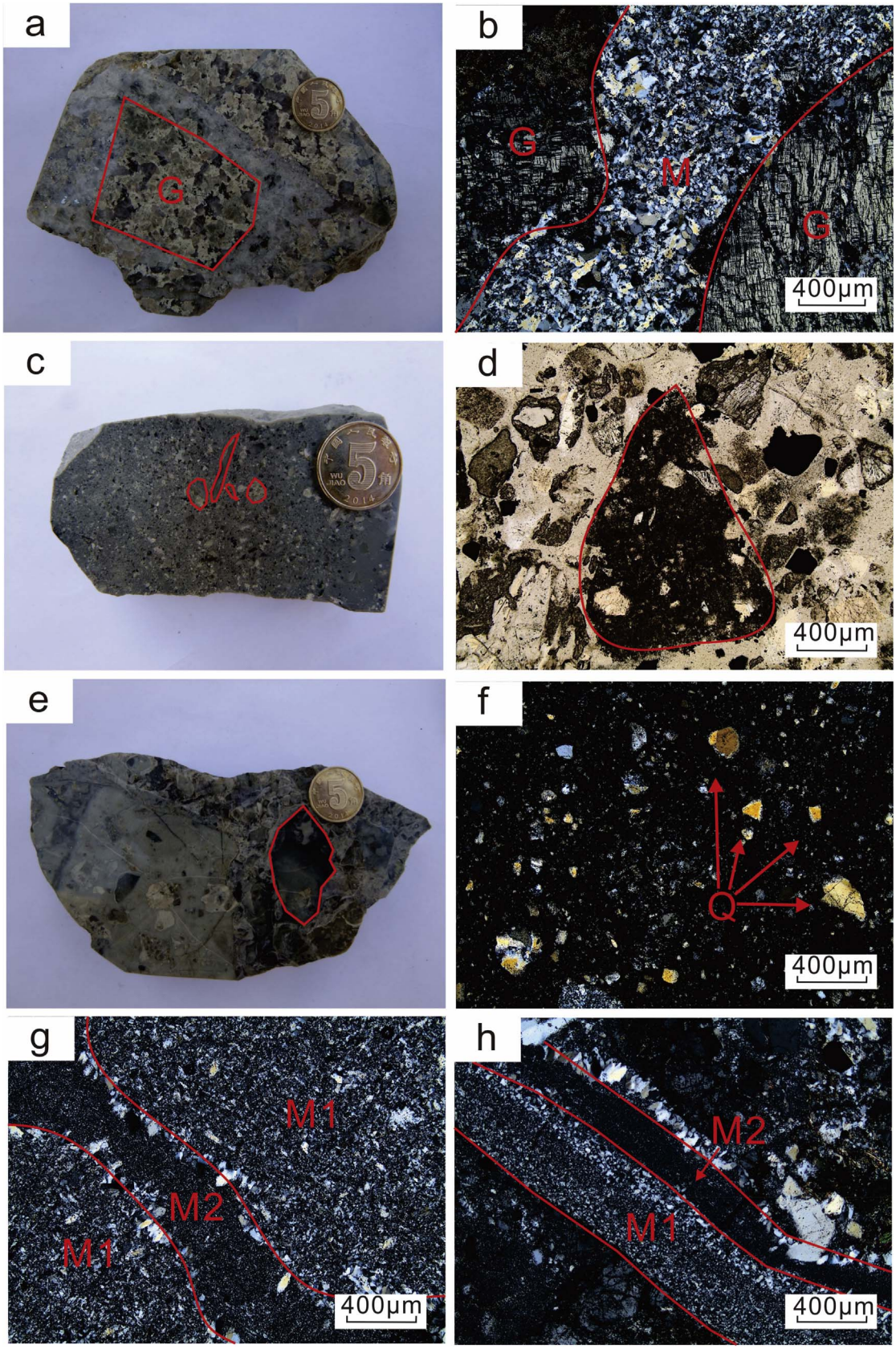

Fig. 3. The breccias from the Niujuan silver deposit. (a) and (b) Photograph and photomicrograph (under transmitted light) of the breccia, the fragments of which constitute the granite rock debris. (c) and (d) Photograph and photomicrograph (under transmitted light) of the breccias with tuff rock debris as fragment. (e) Photograph of angular fragments in the silicic breccias. (f) Photomicrograph (under transmitted light) of the crystal fragment of quartz. (g) and (h) The former cementing material re-cemented at a later stage. Q-Quartz, G-Granite, M1-Former cement M2-Later cement.

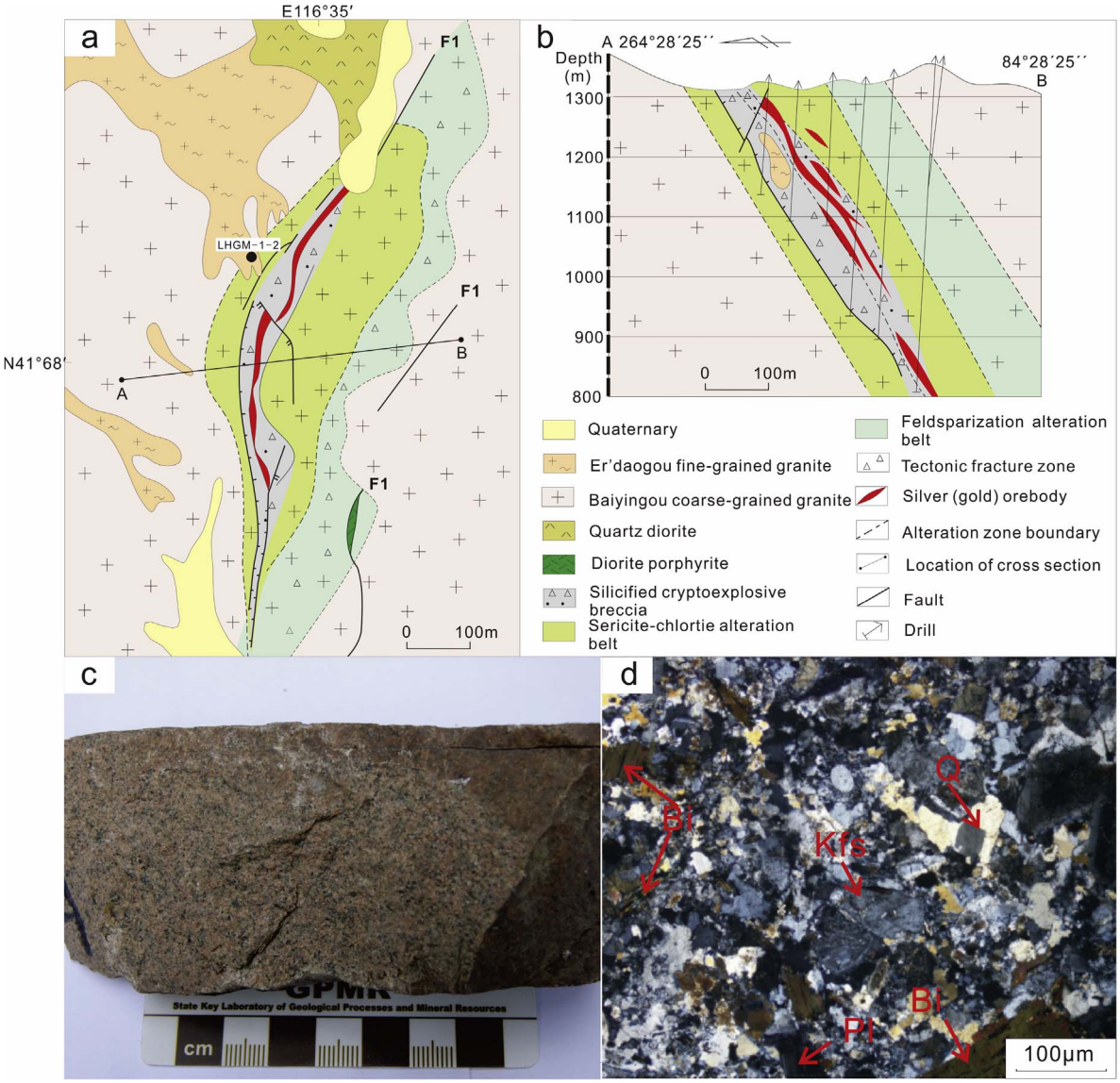

Fig. 4. (a) Geological map of the Niujuan silver deposit after (Li et al., 2006). (b) Geological cross section of the Niujuan silver deposit. (c) Hand specimen photograph of the sample (LHGM-1-2) collected for zircon U–Pb dating. (d) The major mineral assemblages in the sample of present study. Pl-plagioclase; Kfs-K-feldspar; Q-quartz; Bi-biotite.

(Fig. 5). Pyrite occurs as coarse-grained, idiomorphic (Fig. 5a) or hypidiomorphic grains (Fig. 5b), mainly as cubic crystals with a faint yellow color. Pyrite is generally replaced by galena and sphalerite (Fig. 5c, d). Small chalcopyrite grains are disseminated in the crystallographic directions of sphalerite (Fig. 5e, f). The gangue minerals are chalcedony, quartz, sericite, feldspar and fluorite, with minor chlorite, calcite, apatite and biotite.

Microscopy observation and BSE images have revealed eleven types of silver minerals, among which native silver and argentite are the most common types (Fig. 5g, h). In addition, some lead- and zinc-bearing argentites also occur in altered sulfides which were replaced by the later-formed silver minerals (Fig. 5g, h).

3.5. Wall rock alterations and hydrothermal events

Silver mineralization in the Niujuan deposit is associated with intense hydrothermal alterations, including silicification, K-feldspathization, sericitization, kaolinization, montmorillonitization, chloritization and carbonatization, comprising a variety of alteration minerals such as K-feldspar, sericite, chlorite, montmorillonite and kaolinite. The hydrothermal alteration shows marked zoning (Fig. 4a, b). From the Niujuan-Laohuba fault to the adjoining breccias, three zones of alteration are identified with gradually weakening intensity as: silicification zone (microcrystalline quartz + pyrite + sphalerite + galena) → sericitization-chloritization zone (sericite + quartz + feldspar + pyrite + chlorite) → K-feldspathization zone (K-feldspar + quartz). Silicification shows close relationship with silver mineralization and the silicified rocks consist of chalcedony and quartz. The silicified breccias are the main ore-bearing rocks in the Niujuan silver deposit.

The silver-forming event in the Niujuan deposit involved four stages of hydrothermal activity as follows.

1) Stage I is marked by the occurrence of quartz veins in the host breccias and granite (Fig. 6a). These veins mainly consist of microcrystalline quartz, chalcedony and minor pyrite. The disseminated pyrite is idiomorphic and coarse grained. Minor yellowish green scaly sericite (less than 0.5 mm in size) occurs in the form of microcrystals in quartz (Fig. 6b).
2) Stage II is marked by the occurrence of quartz-pyrite veins ranging in width from 0.5 to 2 cm (Fig. 6c). The quartz formed during this stage is smoky-gray. Cubic pyrite crystals of about 0.5–2 mm size are sparsely disseminated within the quartz (Fig. 6d).

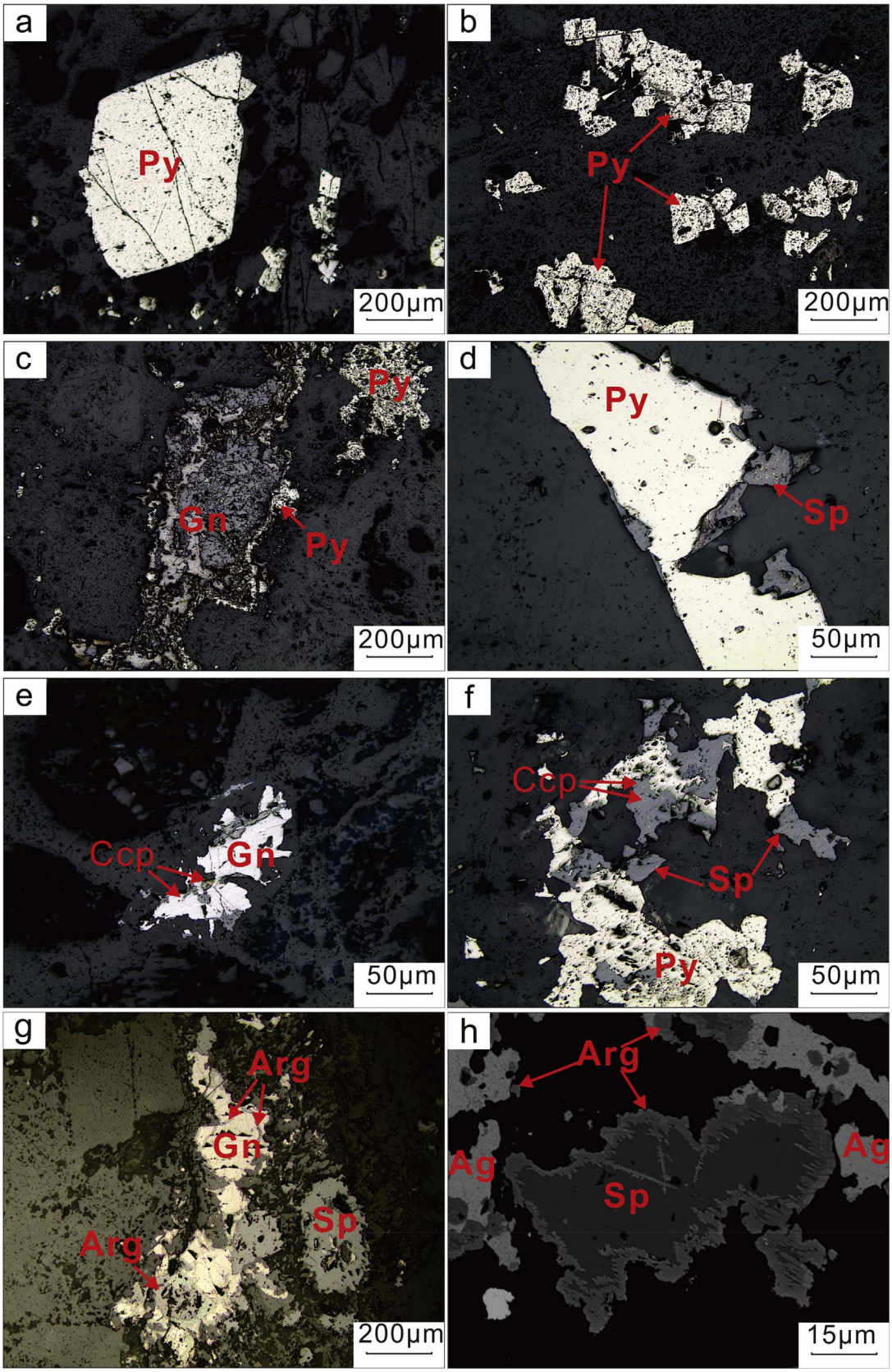

Fig. 5. Representative photomicrographs showing the major metallic minerals of the Niujuan silver deposit. (a) Idiomorphic pyrite. (b) Hypidiomorphic pyrite. (c) Pyrite replaced by galena. (d) Pyrite replaced by sphalerite. (e) and (f) Chalcopyrite exsolution showing different textures in sphalerite grains. (g) Argentite in sphalerite and in the cranny of galena (a-e are under reflective light). (h) Sphalerite replaced by argentite (BSE image). Py-pyrite; Gn-galena; Sp-sphalerite; Ccp-chalcopyrite; Arg -Argentite; Ag-native silver.

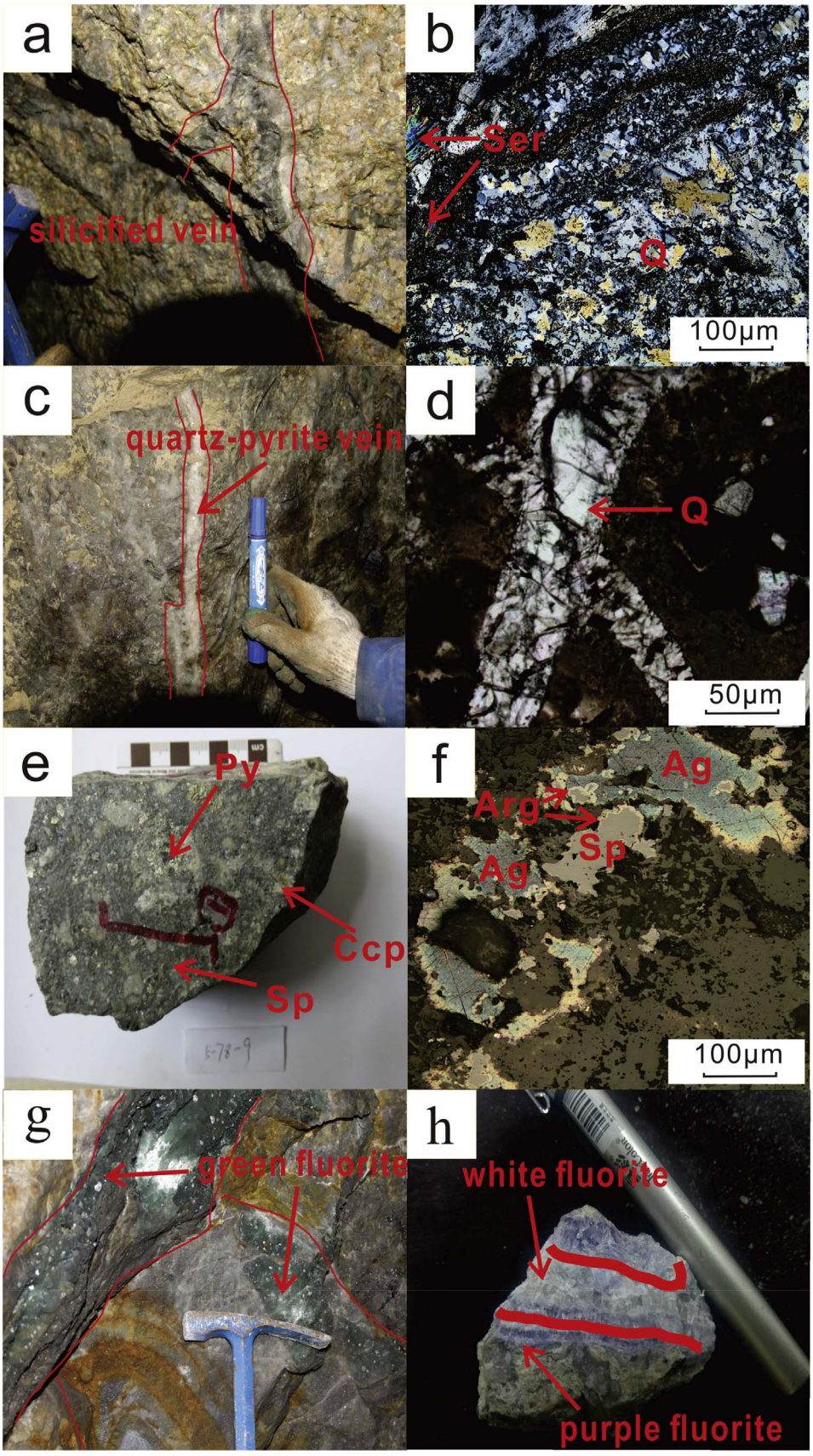

Fig. 6. Photographs showing the characteristics of the hydrothermal stages of the Niujuan silver deposit. (a) Stage I silicified vein cutting the wall rocks. (b) Stage I silicified vein mainly consist of quartz. (c) Stage II quartz-pyrite vein. (d) Stage II quartz is coloured in smoky-gray. (e) and (f) Stage III polymetallic sulfides. (g) Stage IV green fluorite vein. (h) Stage IV white and purple fluorite veins. Q-quartz; Py-pyrite; Sp-sphalerite; Ccp-chalcopyrite; Ser-sericite; Arg-Argentite; Ag-native silver.

3) Stage III is characterized by sulfides mainly including pyrite, galena, sphalerite and argentite (Fig. 6e). Native silver and argentite also occur in this stage (Fig. 6f). Silver mineralization shows a close relationship to the stage III hydrothermal event.
4) Stage IV is marked by fluorite veins interwoven with the early stage mineral assemblages (Fig. 6g). This stage is divided into 3 sub-stages

in accordance with the color of fluorite such as purple fluorite sub-stage, green fluorite sub-stage and white fluorite sub-stage (Fig. 6h).

4. Sampling and analytical methods

4.1. Sampling

A representative sample (LHGM-1-2) of the Er'daogou granite was used for zircon geochronology using LA-ICPMS (Fig. 4c). The sample exhibits massive texture and is mainly composed of K-feldspar (ca. 42%), quartz (ca. 30%), plagioclase (ca. 20%) and biotite (ca. 5%) (Fig. 4d), with minor accessory minerals including apatite, magnetite, titanite and zircon.

Samples for isotopic analyses were collected mainly from the underground mine at a depth of 1150–1190 m in the Niujuan silver deposit. All the mineral samples for the S, Pb, He and Ar isotopic analyses were selected from the main stages (i.e., stage II and stage III). The quartz samples for H–O isotopic analyses were selected from stages I and II. Five fluorite samples for Sm–Nd isotopic analyses were selected from stage IV.

Sampling was undertaken to meet the following criteria: (1) to minimize the effect of weathering, (2) to ensure that materials were available from both hanging wall and footwall, and (3) to include representative samples of all the ore types. After crushing and sieving of the representative samples, the separated mineral grains of 40–60 mesh in size were handpicked under a binocular stereo-microscope to ensure > 99% purity.

4.2. Analytical methods

4.2.1. Zircon U-Pb dating

Zircon U-Pb dating was performed on a laser ablation inductively coupled plasma mass spectrometry (LA-ICP-MS) at the National Key Laboratory of Continental Dynamics of Northwest University. The analytical procedures are described in Yuan et al. (2004). The laser spot diameter and frequency were 30 μm and 10 Hz, respectively. Zircon 91500 was employed as the standard and silicate glass NIST was used to optimize the instrument. Raw data were processed using the GLITTER program to calculate isotopic ratios and ages of $^{207}Pb/^{206}Pb$, $^{206}Pb/^{238}U$, $^{207}Pb/^{235}U$, respectively. Data were corrected for common lead, according to the method of Anderson (2002), and ages were computed by ISOPLOT 4.15 software (Yuan et al., 2004).

4.2.2. Sm-Nd isochron age

Sm and Nd isotopic measurements were carried out at the Modern Analysis Center, Nanjing University, and analyzed on a VG-354 ionization mass spectrometer. Details of the chemical separation and mass spectrometric procedures are described by Wang et al. (2007). Simultaneous analysis of the American Standard Reference Material NBS987 gave $^{143}Nd/^{144}Nd$ of 0.511863 ± 0.000006 (2σ). The $^{87}Sr/^{86}Sr$ is normalized to $^{146}Nd/^{144}Nd = 0.7219$, in order to correct for instrumental fractionation.

4.2.3. Sulfur and lead isotopes

Sulfur isotopic compositions were determined with a Finnigan MAT 251 mass spectrometer in the Beijing Research Institute of Uranium Geology, following the procedures outlined by Glesemann et al. (1994). The precision for $\delta^{34}S$ is better than ± 0.2‰ and the data are reported relative to Vienna Canon Diablo Troilite (V-CDT) sulfide. Pb isotopic ratios were analyzed with the same mass spectrometer, with an analytical precision better than ± 0.2‰.

4.2.4. Hydrogen and oxygen isotopes

The hydrogen isotopic compositions of fluid inclusions in quartz and oxygen isotopic compositions of quartz were determined with a Finnigan-MAT253 mass spectrometer. Oxygen was extracted from quartz by the BrF5 method (Clayton and Mayeda, 1963), and hydrogen isotopic compositions of fluid inclusions were analyzed using the Zn reduction method (Coleman et al., 1982). The analytical precisions were better than ± 0.2‰ for $\delta^{18}O$ quartz and ± 1‰ for δD. The values of $\delta^{18}O$ and δD are reported as ‰ deviation from SMOW and V-SMOW, respectively.

4.2.5. Noble gas isotopic geochemistry

He-Ar isotopic compositions were determined with a MM5400 mass spectrometer (Micromass, GB) in the Beijing Research Institute of Uranium Geology. The analyses were performed with electric current of It4 = 800 μA, It40 = 200 μA, and 9000 kV. Samples were weighed and transferred to aluminum foil, and loaded in an all-metal extraction system for noble gas analysis. The background value for 1600 °C was $^{4}He = 1.10 \times 10^{-14}$, $^{40}Ar = 6.21 \times 10^{-13}$ in unit mol. The standard sample (air) for the experiments was from the summit of Gaolan Mountain, Lanzhou, China. The analytical precision for the noble gas isotopic measurements is better than 10%, adopting procedures reported in earlier studies (Ye et al., 2007; Sun et al., 2009).

5. Results

5.1. Zircon U-Pb ages

The zircon U-Pb data from the Er'daogou fine-grained K-feldspar granite in the Niujuan silver deposit are listed in Table 1. The zircon crystals are mostly euhedral, transparent and colorless. The majority of the grains exhibit oscillatory or planar zoning in CL (Fig. 7), indicating their magmatic origin (Corfu et al., 2003). The thorium and uranium contents range from 124.53 to 1018.43 ppm and from 83.88 to 567.71 ppm, with corresponding Th/U ratios of 0.983–1.794. The high Th/U ratios of the zircon grains also indicate their magmatic crystallization history (Hoskin and Schaltegger, 2003). Thirteen spots yield a $^{206}Pb/^{238}U$ weighted mean age of 145.5 ± 2.1 Ma (95% conf., MSWD = 2.1, n = 13; Fig. 8a), which is consistent with the concordia age of 143 ± 7 Ma (Fig. 8b). The Late Jurassic age is considered to represent the formation age of the Er'daogou fine-grained K-feldspar granite.

5.2. Sm-Nd isochron age

The Sm and Nd isotopic data of stage IV fluorites are listed in Table 2. The Sm and Nd contents of the samples are relative high, ranging from 1.607×10^{-6} to 16.93×10^{-6} and from 8.437×10^{-6} to 12.92×10^{-6}, with $^{147}Sm/^{144}Nd$ and $^{143}Nd/^{144}Nd$ ratios of 0.0851–0.7927 and 0.511859–0.512506. Data regression for isochron age and weighted mean value were done with the Isoplot/Ex version 3.00 (Ludwig, 2003), using 2% error for $^{147}Sm/^{144}Nd$ ratios and the within-run measurement precision for $^{143}Nd/^{144}Nd$ values (2σ). The data yielded an isochron age of 139.2 ± 3.8 Ma (MSWD = 2.8) with an initial $^{147}Sm/^{144}Nd$ ratio of 0.511785 ± 0.00011 (Fig. 9). Anglin et al. (1996) showed that Sm-Nd isotopic dating can be reliably applied in hydrothermal systems assuming consanguinity, synchronism and sealing. Sm and Nd have a very low diffusion rate and the Sm-Nd isotopic system normally remains sealed after the precipitation of fluorite from hydrothermal system. Thus the Sm-Nd isochron age (139.2 ± 3.8 Ma) represents the formation age of stage IV fluorites.

5.3. S and Pb isotopic composition

Results of sulfur isotopic analyses are presented in Table 3. The $\delta^{34}S$ values of sulfide samples (including three stages II and III pyrite samples, two stage III galena samples and two stage III sphalerite samples) range from 2.4‰ to 5.3‰ with the mean value of 3.8‰. The mean $\delta^{34}S$ values of pyrite, galena and sphalerite are 3.6‰, 2.8‰ and 5.3‰, respectively. The $\delta^{34}S$ values of the Er'daogou fine-grained K-feldspar

Table 1
LA-ICP-MS zircon U-Pb isotopic data of the Er'daogou fine-grained K-feldspar granite in the Niujuan silver deposit.

Spot	Conc. (ppm)			Isotope ratio							Age (Ma)					
	Th	U	Th/U	$^{207}Pb/^{206}Pb$	1σ	$^{207}Pb/^{235}U$	1σ	$^{206}Pb/^{238}U$	1σ	$^{207}Pb/^{206}Pb$	1σ	$^{207}Pb/^{235}U$	1σ	$^{206}Pb/^{238}U$	1σ
LHGM-1-2-01	374.50	364.10	1.028564	0.05133	0.00590	0.16662	0.01825	0.02361	0.00068	255.5	244.33	156.5	15.88	150.4	4.26
LHGM-1-2-08	241.64	222.70	1.085047	0.05442	0.00531	0.16483	0.01515	0.02201	0.00055	388.5	205.47	154.9	13.21	140.3	3.50
LHGM-1-2-09	181.52	184.71	0.982730	0.05290	0.00396	0.16203	0.01111	0.02226	0.00046	324.5	160.85	152.5	9.71	141.9	2.87
LHGM-1-2-10	1018.43	567.71	1.793926	0.04947	0.00237	0.14582	0.00568	0.02142	0.00036	170.0	108.33	138.2	5.04	136.6	2.29
LHGM-1-2-11	348.51	327.23	1.065031	0.05146	0.00296	0.16018	0.00799	0.02261	0.00041	261.4	126.80	150.9	6.99	144.2	2.58
LHGM-1-2-14	211.77	181.33	1.167871	0.04940	0.00646	0.15654	0.01965	0.02301	0.00072	166.8	279.60	147.7	17.25	146.7	4.51
LHGM-1-2-15	124.53	108.04	1.152629	0.05253	0.00713	0.16528	0.02160	0.02285	0.00071	308.5	282.66	155.3	18.82	145.6	4.47
LHGM-1-2-16	248.13	205.88	1.205217	0.05180	0.00432	0.16826	0.01303	0.02358	0.00052	276.7	180.00	157.9	11.33	150.2	3.27
LHGM-1-2-17	227.16	225.09	1.009196	0.05232	0.00337	0.16554	0.00951	0.02297	0.00044	299.4	140.21	155.5	8.28	146.4	2.78
LHGM-1-2-18	455.20	394.32	1.154392	0.05355	0.00274	0.16947	0.00722	0.02297	0.00040	352.2	110.78	159.0	6.27	146.4	2.54
LHGM-1-2-19	219.90	125.99	1.745377	0.05450	0.00463	0.16854	0.01332	0.02244	0.00050	391.9	180.00	158.2	11.58	143.1	3.18
LHGM-1-2-21	651.83	565.55	1.152559	0.04753	0.00229	0.14820	0.00584	0.02263	0.00038	75.1	111.43	140.3	5.17	144.2	2.39
LHGM-1-2-23	171.41	170.41	1.005868	0.05084	0.00398	0.16657	0.01207	0.02377	0.00049	233.5	171.37	156.4	10.51	151.4	3.06

granites range from −0.5‰ to 5‰ and from −0.9‰ to 7.7‰, respectively.

Lead isotopic data are listed in Table 4. The sulfide samples exhibit $^{206}Pb/^{204}Pb$, $^{207}Pb/^{204}Pb$ and $^{208}Pb/^{204}Pb$ values of 16.837–16.932 (average 16.894), 15.420–15.501 (average 15.477) and 37.599–37.953 (average 37.785), respectively. The corresponding lead isotopic values of the Er'daogou fine-grained K-feldspar granite are respectively 17.258–17.821, 15.384–15.544 and 37.899–38.271, which are similar to the values of the Baiyingou coarse-grained K-feldspar granite ranging from 17.187 to 18.023, from 15.432 to 15.541, and from 37.492 to 38.502, respectively.

5.4. H–O isotopic composition

Hydrogen and oxygen isotopic analytical data of quartz are listed in Table 5. The $\delta^{18}O_Q$ values of ten samples (three samples come from this study, and the rest are from previous studies) range from 0.6‰ to 4.15‰ (average 2.53‰), and the $\delta^{18}D_w$ values range from −119.4‰ to −98.7‰ (average −108.9‰). The oxygen isotopic composition of the ore-forming fluid ($\delta^{18}O_w$) can be calculated from that of quartz with the equation $1000\ \ln\alpha_{Q\text{-}W} = 3.38 \times 10^6 T^{-2} - 3.40$ (Clayton, 1972), where T represents the formation temperature of fluid inclusions in quartz. The $\delta^{18}O_w$ values of the mineralizing fluids have a range from −7.05‰ to −2.74‰, with an average of −4.51‰.

5.5. He-Ar isotopic composition

Helium and argon isotopic data on the Niujuan silver deposit are listed in Table 6. The $^3He/^4He$ ratios of the inclusions in pyrite are in the range 0.921–4.81Ra (Ra is the $^3He/^4He$ ratio of air = 1.4×10^{-6}) with a mean value at 2.239Ra. The results fall between crustal $^3He/^4He$ (0.01–0.05 Ra) and mantle $^3He/^4He$ (6–7 Ra). The $^{40}Ar/^{36}Ar$ ratios show variation from 299.34 to 303.84 with an average of 301.97, which is higher than the $^{40}Ar/^{36}Ar$ value of the atmosphere (295.5).

6. Discussion

6.1. Timing of the ore mineralization

The emplacement time of the Baiyingou granite as constrained from the zircon U-Pb age of 241 ± 0.08 Ma (Li and Wang, 2002), is consistent with the Triassic granitic magmatism in North Hebei (245–194 Ma; Liu and Zhang, 1997). The Er'daogou granite, yielding a zircon U-Pb age of 145.5 ± 2.1 Ma, formed during the Yanshanian period, markedly later than the Baiyingou granite, which is also supported by the intrusion of Er'daogou granite into the Baiyingou granite (Fig. 2). The orebodies of the Niujuan silver deposit are hosted in breccias, with angular fragments of both Baiyingou and Er'daogou granites. Thus the zircon U-Pb age of 145.5 ± 2.1 Ma for Er'daogou granite is taken as the lower limit of the Niujuan silver mineralization age.

The Sm-Nd age of hydrothermal mineral assemblages has been used to precisely constrain the time of mineralization (Liu et al., 1998; Peng et al., 2006). As a typical hydrothermal mineral, fluorite occurs widely in different hydrothermal ore deposits (Duane et al., 1991; Cook and Ciobanu, 2005; Zhao et al., 2005; McPhie et al., 2011), and the associated metal enrichment is generally attributed to the precipitation of metallic minerals from ore-forming fluids (Seward and Barnes, 1997). Based on a comparative study on fluorine-rich hydrothermal fluids between the Olympic Dam Fe oxide-Cu-U-Au-Ag deposit and the Guilaizhuang gold deposit, Xu et al. (2015) argued that the fluorine related with the formation of cryptoexplosive ore-bearing breccias obviously contributed to the mineralization. Similarly, the fluorite in the Niujuan silver deposit shows high content of silver. Given that fluorine is a powerful ligand for metal transportation like OH^-, Cl^- and HS^- (Wood and Samson, 1998; Pirajno, 2009), the upwelling of F-rich

Fig. 7. CL images of zircons from the Er'daogou granite, showing the analytical spots.

hydrothermal fluids is inferred to have substantially precipitated metals in the fractures of breccias, leading to the formation of fluorite during the final hydrothermal stage. Thus the Sm-Nd isochron age of 139.2 ± 3.8 Ma for the stage IV fluorite, formed slightly later than the silver mineralization, marks the upper limit of the silver mineralization age.

The zircon U-Pb age and fluorite Sm-Nd isochron age suggest a close relationship between the formation of the Niujuan silver deposit and the intrusion of the Er'daogou granite, whereas the Baiyingou granite did not play any major role in the mineralization.

6.2. Sources of ore-forming materials and fluids

The stable isotopic composition of sulfide minerals is a useful tool to constrain the origin of hydrothermal fluids. Sulfur isotopic composition of the hydrothermal system is determined by the physicochemical conditions including temperature, pH value, oxygen fugacity and ion activity (Sakai, 1968; Ohmoto and Rye, 1979; Hoefs, 1997). However, under reduced hydrothermal condition where H_2S is the dominant sulfur species in the fluid, the average $\delta^{34}S$ values of sulfide minerals approximate the $\delta^{34}S$ value of hydrothermal fluid (Ohmoto and Rye, 1979).

In the Niujuan silver deposit, the dominant sulfide minerals formed during stage III are pyrite, galena and sphalerite, indicating a relatively simple paragenesis. The average $\delta^{34}S$ values of sulfide minerals, therefore, can directly represent the sulfur source. The $\delta^{34}S$ range of 2.4–5.3‰ (averaging at 3.68‰) of the Niujuan silver deposit is close to those of meteorite and mantle, suggesting a homogeneous source with the involvement of mantle-derived components during the ore-forming processes (Ohmoto, 1972; Saravanan and Mishra, 2009). The $\delta^{34}S$ values of the Er'daogou and Baiyingou granite samples (−0.5‰ to 5‰ and −0.9‰ to 7.7‰), suggest a genetic relationship between the ore-forming fluid and the Mesozoic intrusions. In contrast, the $\delta^{34}S$ value of pyrite in granulite from the Hongqiyingzi group is estimated at 10.5‰ (Hu, 1990), which is markedly higher than the values for the ore sulfides, further suggesting that the ore-forming fluids do not have any

Table 2
Fluorite Sm–Nd analytical data of the Niujuan silver deposit.

Sample no.	Mineral	Sm(ug/g)	Nd(ug/g)	$^{147}Sm/^{144}Nd$	$^{143}Nd/^{144}Nd$	2σ
5-73-Y	White fluorite	5.924	9.305	0.3854	0.512139	8
5-CM31-Y	Purple fluorite	1.607	11.43	0.0851	0.511859	9
9-80N-Y	White fluorite	3.529	11.28	0.1896	0.511962	6
9-75N-Y	Green fluorite	4.316	8.437	0.3182	0.512071	7
9-72-Y	White fluorite	16.93	12.92	0.7927	0.512506	8

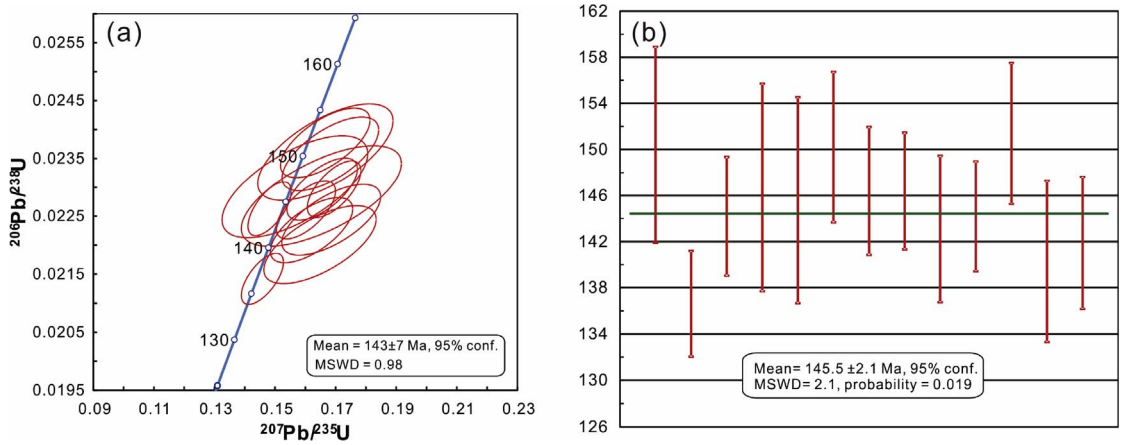

Fig. 8. Zircon U-Pb concordia plots (a) and recalculated weighted mean $^{206}Pb/^{238}U$ ages (b) for the Er'daogou granite.

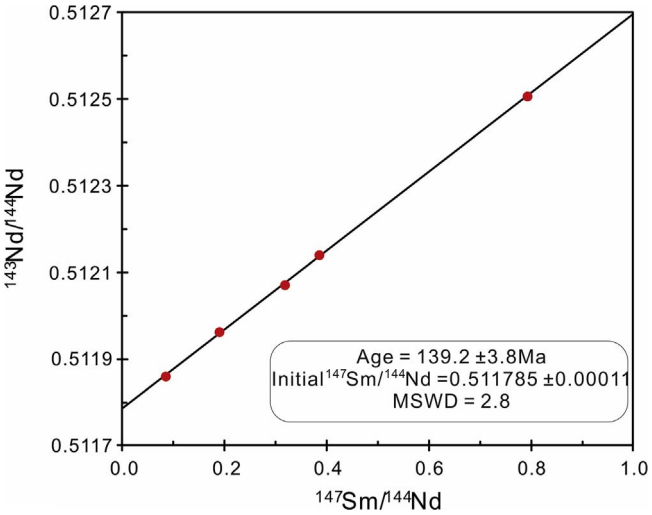

Fig. 9. Sm-Nd isochron age for the stage IV fluorite from the Niujuan silver deposit.

Table 3
Sulfur isotopic composition of sulfides from the Niujuan silver deposit.

Location	Sample No.	Stage	Mineral	δ^{34}SVCDT (‰)
Niujuan silver deposit	1-73-5	II	Pyrite	2.6
	1-77-6	II	Pyrite	3.6
	5-71-3	III	Pyrite	4.7
	5-73-5(Gn)	III	Galena	2.4
	5-73-5(Sp)	III	Sphalerite	5.2
	5-73-4(Sp)	III	Sphalerite	5.3
	5-73-4(Gn)	III	Galena	3.1
Intrusions	FNγX1	Er'daogou fine-grained K-feldspar granite	Whole rock	−0.5
	Zk74-25	Er'daogou fine-grained K-feldspar granite	Whole rock	5.0
	YSG-2	Baiyingou coarse-grained K-feldspar granite	Whole rock	7.7
	DB-1	Baiyingou coarse-grained K-feldspar granite	Whole rock	−0.9

major relationship with the basement rocks (Fig. 10).

The Pb isotopic compositions of the sulfides from the Niujuan sliver deposit show a restricted range in the lead isotope evolution diagrams

Table 5
Oxygen and hydrogen isotopic compositions of quartz from the Niujuan silver deposit.

Sample No.	Stage	Mineral	$\Delta D_{V\text{-}SMOW}$ (‰)	$\delta^{18}O_{V\text{-}SMOW}$ (‰)	$\delta^{18}O_w$ (‰)	T(°C)	Reference
1-79-4	II	Quartz	−104.3	0.60	−7.05	280	This study
9-78-2	II	Quartz	−113.2	2.50	−5.15	280	
9-72-4	I	Quartz	−119.4	3.00	−3.89	300	
82lineCM3	I	Quartz	−98.70	1.31	−5.58	300	
ZK83-1	I	Quartz	−104.8	2.78	−4.11	300	
ZK79-3	I	Quartz	−116.9	2.62	−4.27	300	
82lineCM3	I	Quartz	−105.0	4.15	−2.74	300	Li and Geng (1997)
82lineCM3	I	Quartz		2.13	−4.76	300	
TC80	I	Quartz		2.21	−4.68	300	
TC82	I	Quartz		4.01	−2.88	300	

(Zartman and Doe, 1981). The Pb isotopic data for sulfides plot close to orogenic belt curve in Fig. 11a, suggesting that the Pb reservoir was derived from crustal sources of the northern margin of the North China Craton. In Fig. 11b, all the data plot between the mantle and lower crust evolution lines, suggesting a deep-seated source.

Zhu (1998) proposed a Δβ–Δγ diagram based on the ranges of Δβ and Δγ values of lead from various types of rocks and ores (Fig. 12). The Δβ and Δγ values are calculated according to the equations $\Delta\beta = (\beta - \beta_M) \times 1000/\beta_M$ and $\Delta\gamma = (\gamma - \gamma_M) \times 1000/\gamma_M$ (β: $^{207}Pb/^{204}Pb$ of sample, β_M: $^{207}Pb/^{204}Pb$ of mantle, γ: $^{208}Pb/^{204}Pb$ of sample, γ_M: $^{208}Pb/^{204}Pb$ of mantle; Zhu, 1998). The age of silver mineralization is taken as 139 Ma to calculate the Δγ and Δβ values. The Δγ − Δβ diagram (Fig. 12) indicates a mantle source of lead for the Niujuan silver deposit.

Oxygen and hydrogen isotopes are also potential tracers of the source of hydrothermal fluids (Clayton, 1972). In spite of the isotopic exchange during water-rock reaction associated with large-scale hydrothermal alteration, the early-stage fluid can be used to constrain the original source composition (Guo et al., 2014; Liu et al., 2015). Thus the δD and $\delta^{18}O$ values of the stages I and II quartz samples are considered to constrain the origin of the ore-forming fluids in the Niujuan deposit.

In Fig. 13, the δD and $\delta^{18}O$ values plot between the meteoric water line and the range of primary magmatic water, suggesting that magmatic water played an important role in the silver mineralization. In addition, the sliver orebodies are located along zones that show intense water-rock reaction between ore-forming fluid and granite, which might have led to the significant variations in oxygen and hydrogen

Table 4
Lead isotopic composition of sulfides from the Niujuan silver deposit.

Location	Sample No.	Stage	Mineral	$^{206}Pb/^{204}Pb$	$^{207}Pb/^{204}Pb$	$^{208}Pb/^{204}Pb$	Δβ	Δγ
Niujuan silver deposit	1-73-5	II	Pyrite	16.930	15.501	37.872	11.52	17.26
	1-77-6	II	Pyrite	16.932	15.477	37.800	9.96	15.32
	5-71-3	III	Pyrite	16.925	15.499	37.860	11.39	16.94
	5-73-5(Gn)	III	Galena	16.837	15.445	37.665	7.87	11.70
	5-73-5(Sp)	III	Sphalerite	16.917	15.531	37.953	13.48	19.43
	5-73-4(Sp)	III	Sphalerite	16.875	15.465	37.748	9.17	13.93
	5-73-4(Gn)	III	Galena	16.841	15.420	37.599	6.24	9.93
Intrusions	YSG-2	Baiyingou coarse-grained K-feldspar granite	Whole rock	17.668	15.486	38.409	11.05	36.55
	BSLZ-4-1	Baiyingou coarse-grained K-feldspar granite	Whole rock	17.389	15.475	37.833	10.33	21.00
	DB-1	Baiyingou coarse-grained K-feldspar granite	Whole rock	18.023	15.541	38.502	14.64	39.06
	SWP-5	Baiyingou coarse-grained K-feldspar granite	Whole rock	17.187	15.432	37.492	7.52	11.80
	ZK76-10-1	Baiyingou coarse-grained K-feldspar granite	Whole rock	17.957	15.540	38.344	14.57	34.79
	FNγX1	Er'daogou fine-grained K-feldspar granite	Whole rock	17.668	15.484	38.180	10.41	25.44
	LHGM-2-1	Er'daogou fine-grained K-feldspar granite	Whole rock	17.258	15.384	37.889	3.88	17.62
	LTC-4	Er'daogou fine-grained K-feldspar granite	Whole rock	17.821	15.544	38.271	14.32	27.88
	ZK74-25	Er'daogou fine-grained K-feldspar granite	Whole rock	17.649	15.500	38.085	11.45	22.89

Table 6
Helium and argon isotopic compositions of the pyrite from the Niujuan silver deposit.

Sample No.	Mineral	^{4}He(cm^{3}STP/g) (10^{-7})	^{40}Ar(cm^{3}STP/g) (10^{-7})	^{3}He/^{4}He (10^{-6})	^{40}Ar/^{36}Ar	3He(cm^{3}STP/g) (10^{-12})	^{36}Ar(cm^{3}STP/g) (10^{-7})	F^{4}He	He$_{mantle}$(%)
1-77-6	Pyrite	1.26	0.843	1.38	303.84	1.7388	0.002774	2744.0367	12.38
5-71-3	Pyrite	0.09	0.967	1.29	299.34	0.1161	0.003230	168.33823	11.56
9-75-1	Pyrite	0.10	0.753	6.74	302.75	0.0674	0.002487	24.293547	61.20

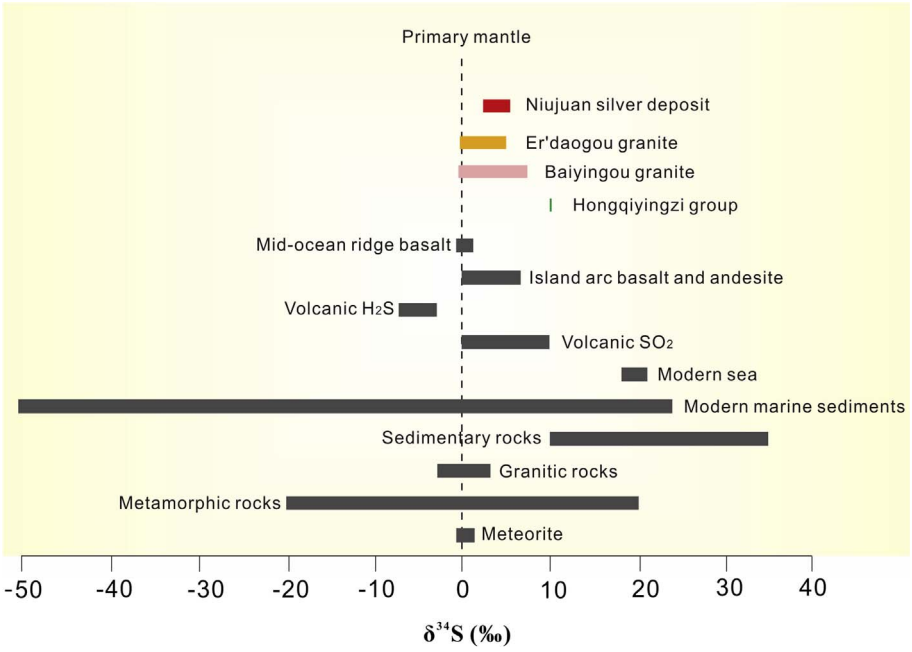

Fig. 10. Sulphur isotopic compositions of sulfides, granites and basement rocks.

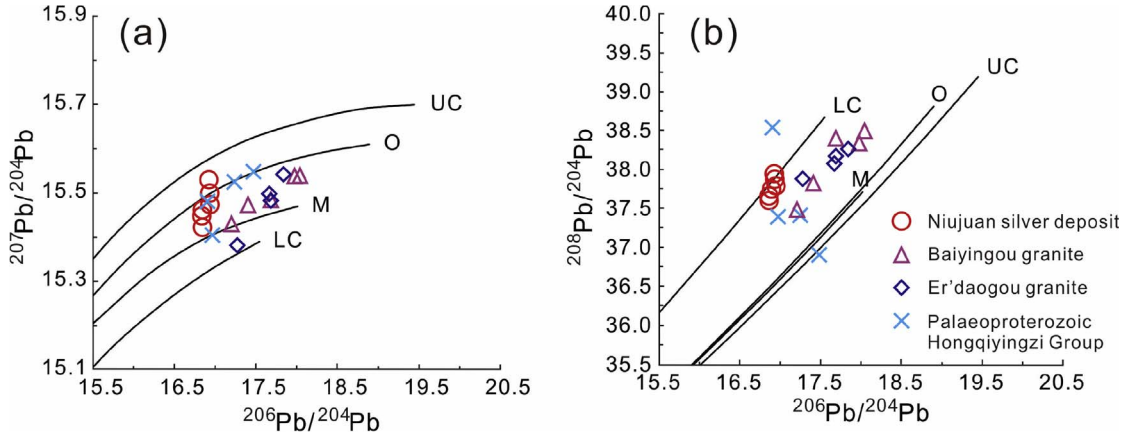

Fig. 11. Lead isotopic composition of sulfides from the Niujuan silver deposit. The Pb tectonic model models after Zartman and Doe (1981): O = orogen; M = mantle; UC = upper crust contributed to the orogen; LC = lower crust contributed to the orogen. Dotted curves show the lead evolutions fit the data.

isotopes. The samples from early to later stages show a trend towards meteoric water line, suggesting the interaction of meteoric water in the later stage. We infer that the ore-forming fluid was derived from magmatic sources and was mixed with meteoric water, resulting in the decrease of δD and $\delta^{18}O$ values of the ore-forming fluid.

Pyrite is an ideal mineral that preserves noble gases associated with the mineralizing fluids (Hu et al., 1997; Zheng and Chen, 2000). The helium content of the hydrothermal fluid can be preserved in fluid inclusions after the formation of mineral (Burnard et al., 1999). Because of the extremely low contents, noble gases in atmosphere would not visibly contaminate the helium composition in crustal fluid (Stuart et al., 1995). In this study, the pyrite samples display no evidence for later deformation; therefore, the helium and argon isotopic values in the inclusions in pyrite are thought to reflect the nature of ore-forming fluids.

The ^{3}He-^{4}He data of fluid inclusions in the stage III pyrite from the Niujuan silver deposit (0.921–4.81 Ra) are distributed in the transition zone between crustal and mantle helium values (Fig. 14a; Stuart et al., 1995; Yamamoto et al., 2009). When plotted in R/Ra vs. ^{40}Ar/^{36}Ar diagram (Fig. 14b), the data points are distributed close to mantle helium domains and the region of atmospheric saturation water. The percentage of mantle helium in hydrothermal fluid in crust-mantle dual model can be calculated based on the equation: $He_{mantle}(\%) = 100 \times (R - Rc)/(Rm - Rc)$, where Rm (^{3}He/^{4}He in

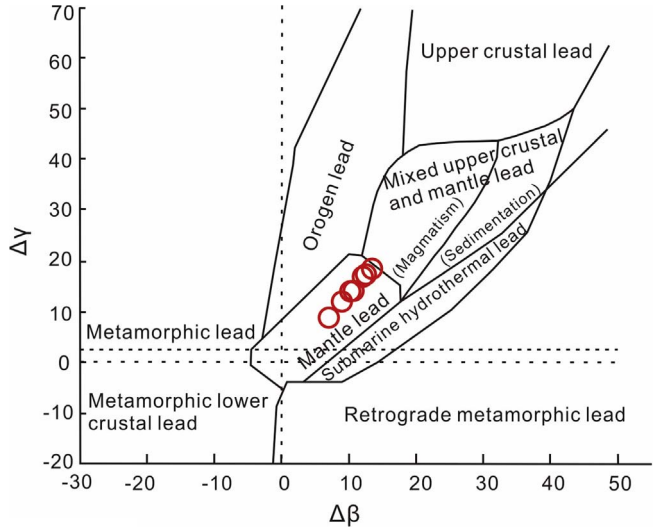

Fig. 12. Δγ–Δβ diagram of ore lead of the Niujuan sliver deposit (after Zhu, 1998).

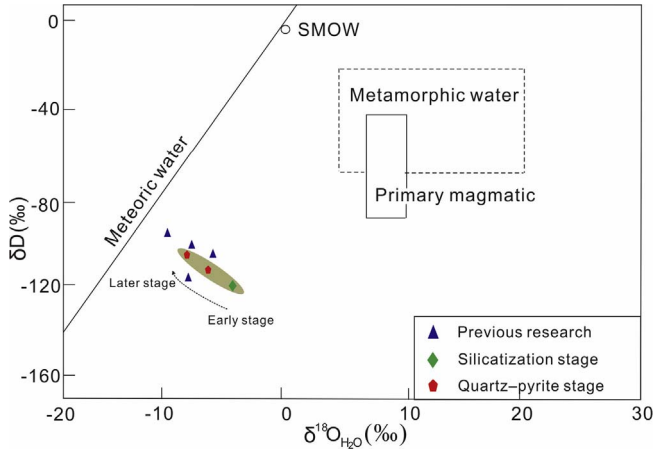

Fig. 13. Hydrogen and oxygen isotopic composition of the Niujuan silver deposit. Data for primary magmatic water, metamorphic water and meteoric water are from Taylor (1974).

mantle) and Rc ($^3He/^4He$ in crust) are set as 1.1×10^{-5} and 2×10^{-8} in this study, respectively (Tolstikhin, 1978; Kendrick et al., 2001; Stuart et al., 1995). The calculated percentage of mantle helium is in the range of 11.56–61.2%. These features suggest that the stage III helium and argon were derived from a mixture of mantle- and atmospheric water-sourced fluid.

Based on the above results, we conclude that the ore-forming fluids in the Niujuan silver deposit might have been derived from subvolcanic plutons and evolved into a mixture of magmatic and meteoric water during the main ore stage. The ore-forming materials were primarily derived from the lower crust with limited input of mantle materials.

6.3. Mechanism of mineralization

After its cratonization, the NCC remained stable until Early Mesozoic when thick neritic clastic rocks and carbonates were deposited on the basement. Large-scale tectonic and magmatic activities took place in the NCC with the formation of substantial quantity of metallic minerals since Mesozoic (Li et al., 2014, 2016; Yang and Santosh, 2015b; Song et al., 2015; He et al., 2016).

Ouyang et al. (2013) proposed that the Mesozoic mineralization in northeastern China and the surrounding regions including North Hebei can be divided into five periods: Triassic (240–205 Ma), Early-Middle Jurassic (190–165 Ma), Late Jurassic (155–145 Ma), Early Cretaceous (140–120 Ma) and late phase of Early Cretaceous (115–100 Ma). The Triassic mineralization was controlled by the post-orogenic extensional setting following the closure of the Paleo-Asian Ocean (Xu et al., 2008; Wang et al., 2012). The Early-Middle Jurassic mineralization was associated with the subduction of the Mongol-Okhotsk oceanic crust and the Paleo-Pacific oceanic plate (Wu et al., 2003; Sun et al., 2010; Chen et al., 2011; Pei et al., 2011). The Late Jurassic mineralization took place during post-orogenic extension following the closure of the Mongol-Okhotsk Ocean (Meng, 2003; Wang et al., 2012; Jahn et al., 2009; Meng et al., 2011; Xu et al., 2013). The Early Cretaceous mineralization occurred within an extensional setting resulting from the closure of the Mongol-Okhotsk Ocean and the subduction of the Paleo-Pacific Plate (Wu et al., 2005; Wang et al., 2006; Zhang et al., 2010; Zhu et al., 2011; Goldfarb and Santosh, 2014). The final phase of Early Cretaceous mineralization is associated with lithospheric extension resulting from asthenospheric upwelling associated with the change in subduction direction of the Paleo-Pacific Oceanic plate (Wu et al., 2007; Sun et al., 2012; Han et al., 2012; Xu et al., 2013; Li and Santosh, 2014, 2017).

The Mesozoic magmatism and mineralization in the North Hebei polymetallic metallogenic belt mainly took place during 200–110 Ma (Li, 2006; Yang, 2000; Li et al., 2011; Li and Santosh, 2014). The Niujuan silver deposit formed between 145.5 ± 2.1 Ma and 139.2 ± 3.8 Ma, during the regional Early Cretaceous mineralization event.

During the Early Cretaceous, owing to the subduction of the Paleo-Pacific Plate and the closure of the Mongol-Okhotsk Ocean, the Niujuan region was in a post-collision extensional setting accompanied by lithospheric delamination, crust-mantle interaction and asthenosphere upwelling (Zhu et al., 2011; Ouyang et al., 2013; Li et al., 2014; Liu

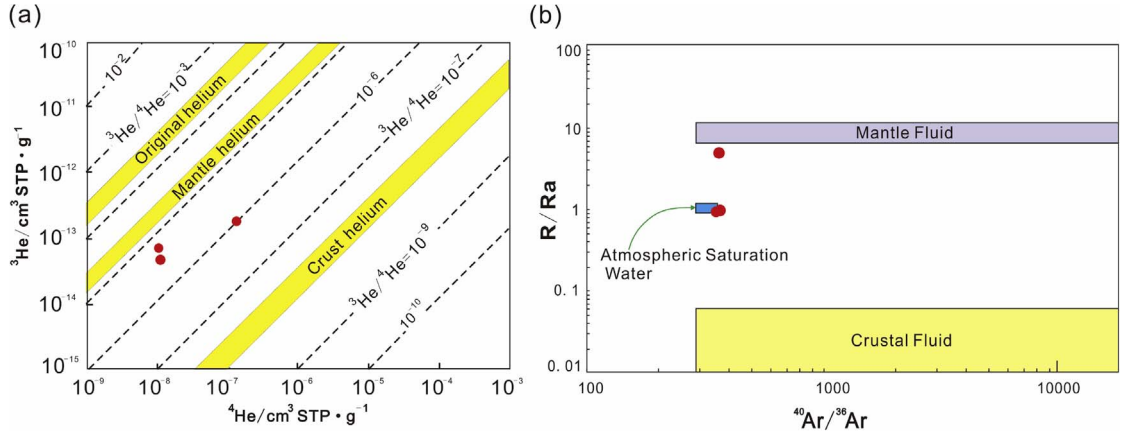

Fig. 14. ^3He-^4He (a) and R/Ra-$^{40}Ar/^{36}Ar$ (b) plots of inclusion-trapped fluids in pyrite from the Niujuan silver deposit (modified from Winckler et al., 2001).

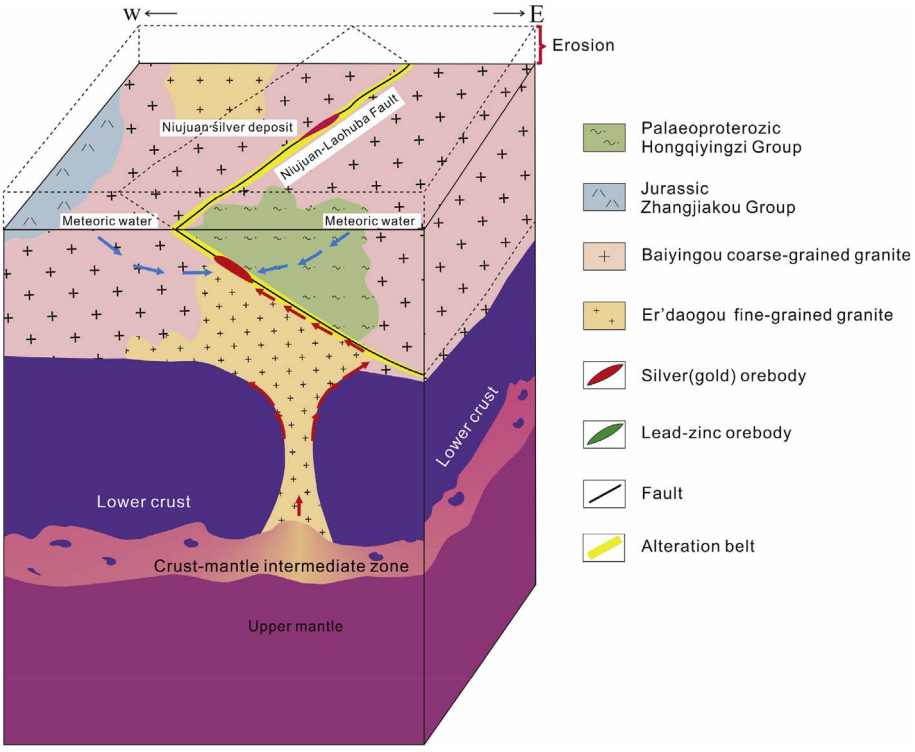

Fig. 15. Metallogenic model for the lode Pb–Zn–Ag deposits in the Niujuan area (modified from Liu and Zhang, 1997).

et al., 2016). These processes resulted in the emplacement of subvolcanic rocks, including the Er'daogou granite and the Baiyingou granite. The residual magma formed during the later event scavenged silver and other elements from the felsic upper crustal rocks. The residual magma, enriched in volatiles, migrated upward along the preexisting faults to shallower levels. The early stage magma that had solidified and produced the Er'daogou granite trapped the residual magmas and with gradual increase in the internal pressure and temperature exceeding the lithostatic pressure, intense cryptoexplosion took place resulting in the formation of cryptoexplosive breccias along the fault zones. In the dilational fractures of cryptoexplosion breccias, the changing physico-chemical conditions such as temperature, pressure, and redox of the mixed fluids resulted in the deposition of sulfides and silver in the Niujuan deposit (Fig. 15).

7. Conclusions

1) Zircon U-Pb dating of the Er'daogou granite from the Niujuan silver deposit yielded an age of 145.5 ± 2.1 Ma, marking the lower limit of the Niujuan silver mineralization. Stage IV fluorites yield a Sm-Nd isochron age of 139.2 ± 3.8 Ma, indicating the upper limit.
2) The ore-forming fluid was originally derived from subvolcanic plutons and evolved into a mixture of magmatic and meteoric water during the main stages. The ore-forming materials were primarily derived from the lower crust with limited input of mantle materials.
3) The Niujuan deposit was formed in an extensional tectonic setting related to the closure of the Mongol-Okhotsk ocean and the subduction of the Paleo-Pacific oceanic plate beneath the North China Craton. The magmatism and metallogeny are correlated to asthenospheric upwelling and crust-mantle interaction with the isotopic data showing mixed crustal melting and mantle sources.

Acknowledgements

We thank Prof. Franco Pirajno, Editor-in-Chief and anonymous referees for their valuable comments and suggestions which improved this paper. We are grateful to the staff in the Fengning Yanshan Mining Limited Liability Company for their help during field work. We also thank Master Course students of our team from China University of Geosciences Beijing for their support during our laboratory work. This work was supported by National Key Research and Development Program of China [2016YFC0600106] and China Geological Survey [12120114051101], and it also get financial supports from the specialized research fund for the doctoral programme of higher education [20130022110003], and the Fundamental Research Funds for the Central Universities (35732015070).

References

Anderson, T., 2002. Correction of common Pb in U-Pb analyses that do not report ^{204}Pb. Chem. Geol. 192, 59–79.
Anglin, C.D., Jonasson, I.R., Franklin, J.M., 1996. Sm-Nd dating of scheelite and tourmaline: implications for the genesis of Archean gold deposits, Val d'Or, Canada. Econ. Geol. 91, 1372–1382.
Babcock Jr, R.C., Ballantyne, G.H., Phillips, C.H., 1995. Summary of the geology of the Bingham district, Utah. Porphyry copper deposits of the American Cordillera: Arizona. Geol. Soc. Digest 20, 316–335.
Burnard, P.G., Hu, R., Turner, G., 1999. Mantle, crustal and atmospheric noble gases in Ailaoshan Gold deposits, Yunnan Province, China. Geochim. Cosmochim. Acta 63, 1595–1604.
Chen, Z.G., Zhang, L.C., Wan, B., Wu, H.Y., Cleven, N., 2011. Geochronology and geochemistry of the Wunugetushan porphyry Cu-Mo deposit in NE China, and their geological significance. Ore Geol. Rev. 43, 92–105.
Clayton, R.N., 1972. Oxygen isotope exchange between quartz and water. J. Geophys. Res. 77, 3057–3607.
Clayton, R.N., Mayeda, T.K., 1963. The use of bromine pentafluoride in the extraction of oxygen from oxides and silicates for isotopic analysis. Geochim. Cosmochim. Acta 27, 43–52.
Coleman, M.L., Sheppard, T.J., Durham, J.J., Rouse, J.E., Moore, G.R., 1982. Reduction of water with zinc for hydrogen isotope analysis. Anal. Chem. 54, 993–995.
Cook, N.J., Ciobanu, C.L., 2005. Tellurides in Au deposits: implications for modelling. In: Mao, J., Bierlein, F.P. (Eds.), Mineral Deposit Research: Meeting the Global Challenge. Springer, Berlin Heidelberg, pp. 1387–1390.
Corfu, F., Hanchar, J.M., Hoskin, P.W., Kinny, P., 2003. Atlas of zircon textures. Rev. Mineral. Geochem. 3, 469–500.
Cunningham, C.G., McNamee, J., Vasquez, J.P., Ericksen, G.E., 1991. A model of volcanic dome-hosted precious metal deposits in Bolivia. Econ. Geol. 86, 415–421.
Duane, M.J., Kruger, F.J., Roberts, P.J., Smith, C.B., 1991. Pb and Sr isotope and origin of Proterozoic base metal (fluorite) and gold deposits, Transvaal Sequence, South Africa. Econ. Geol. 86, 1491–1505.
Fu, C.Y., Gao, B.L., 1998. The structural and geological characteristics of Niuquan silver-gold deposit, Fengning, Hebei Province. J. Geol. Miner. Resour. North China 13,

258–263 (in Chinese with English abstract).
Glesemann, A., Jäger, H.J., Norman, A.L., Krouse, H.R., Brand, W.A., 1994. On-line sulfur-isotope determination using an elemental analyser coupled to a mass spectrometer. Anal. Chem. 66, 2816–2819.
Goldfarb, R.J., Santosh, M., 2014. The dilemma of the Jiaodong gold deposits: are they unique? Geosci. Front. 5, 139–153.
Groves, D.I., Santosh, M., 2016. The giant Jiaodong gold province: the key to a unified model for orogenic gold deposits? Geosci. Front. 7, 409–417.
Guo, L.N., Zhang, C., Song, Y.Z., Chen, B.H., Zhou, Z., Zhang, B.L., Xu, X.L., Wang, Y.W., 2014. Hydrogen and oxygen isotopes geochemistry of the Wang'ershan gold deposit, Jiaodong. Acta Petrol. Sinica 30, 2481–2494 (in Chinese with English abstract).
Han, S.J., Sun, J.G., Bai, L.A., Xing, S.W., Chai, P., Zhang, Y., Yang, F., Men, L.J., Li, Y.X., 2012. Geology and ages of porphyry and medium- to high-sulphidation epithermal gold deposits of the continental margin of Northeast China. Int. Geol. Rev. 55, 287–310.
He, C., Santosh, M., Yang, Q.Y., 2016. Gold metallogeny associated with craton destruction: a geophysical perspective from the north China craton. Ore Geol. Rev. 75, 29–41.
Heinrich, C.A., 2007. Fluid-fluid interactions in magmatic-hydrothermal ore formation. Rev. Mineral. Geochem. 65, 363–387.
Hoefs, J., 1997. Stable Isotope Geochemistry (3nd Edition). Springer Verlag, Berlin, pp. 1–201.
Hoskin, P.W., Schaltegger, U., 2003. The composition of zircon and igneous and metamorphic petrogenesis. Rev. Mineral. Geochem. 53, 27–62.
Hu, R.Z., Bi, X.W., Turner, G., Burnard, P.G., 1997. The system of He-Ar isotope of fluid inclusion in pyrite from the Maguangqing Copper deposit. Sci. China (Ser. D: Earth Sci.) 27, 503–508 (in Chinese with English Abstract).
Hu, X.D., Shen, B.F., Mao, D.B., Zhong, C.T., 2005. On metallogeny of the Caijiaying Pb-Zn deposit. Geol. Surv. Res. 28, 221–227 (in Chinese with English Abstract).
Hu, X.D., 1990. Research of metamorphic complex: second part 'The research methods of metamorphic complex'. Prog. Precambrian Res. 4, 4–62 (in Chinese).
Jahn, B.M., Litvinovsky, B.A., Zanvilevich, A.N., Reichow, M., 2009. Peralkaline granitoid magmatism in the Mongolian-Transbaikalian Belt: evolution, petrogenesis and tectonic significance. Lithos 113, 521–539.
Kendrick, M.A., Burgess, R., Pattrick, R.A.D., Turner, G., 2001. Fluid inclusion noble gas and halogen evidence on the origin of Cu-porphyry mineralizing fluids. Geochim. Cosmochim. Acta 65, 2651–2668.
Kerrich, R., Goldfarb, R.J., Groves, D.I., Garwin, S., Jia, Y.F., 2000. The characteristics, origins and geodynamic settings of supergiant gold metallogenic provinces. Sci. China (Ser. D: Earth Sci.) 43, 1–68.
Li, J.H., Qian, X.L., Huang, X.N., Liu, S.W., 2000. Tectonic framework of North China Block and its cratonization in the early Precambrian. Acta Petrol. Sinica 16, 1–10 (in Chinese with English Abstract).
Li, J.M., 2006. Silver deposits and their metallogenic geodynamics setting in Yanshan area [Doctor's dissertation]. Shenyang, Northeastern University, pp. 34–37 (in Chinese with English abstract).
Li, J.M., Gong, E.P., Yao, Y.Z., Liang, J.H., 2006. The geological-geochemical characteristics and metallogeny of Fengning silver-polymetallic ore deposit, north Hebei province. Contrib. Geol. Miner. Resour. Res. 21, 241–247 (in Chinese with English abstract).
Li, J.M., Ye, Q., Liu, W.J., Wang, Z., 2011. Discussion on metallogenic regularities and dynamics of Mesozoic endogenous non-ferrous metals of Northern Hebei. Miner. Resour. Geol. 25, 98–104 (in Chinese with English abstract).
Li, L., Li, S.R., Santosh, M., Li, Q., Gu, Y., Lü, W.J., Zhang, H.F., Shen, J.F., Zhao, G.C., 2016. Dyke swarms and their role in the genesis of world-class gold deposits: insights from the Jiaodong peninsula, China. J. Asian Earth Sci. 130, 2–22.
Li, L., Santosh, M., Li, S.R., 2015. The "Jiaodong type" gold deposits: characteristics, origin and prospecting. Ore Geol. Rev. 65, 589–611.
Li, S.R., Santosh, M., 2017. Geodynamics of heterogeneous gold mineralization in the North China Craton and its relationship to lithospheric destruction. Gondwana Res. 50, 267–292.
Li, S.R., Santosh, M., 2014. Metallogeny and craton destruction: records from the North China Craton. Ore Geol. Rev. 56, 376–414.
Li, S.R., Santosh, M., Zhang, H.F., Luo, J.Y., Zhang, J.Q., Li, C.L., Zhang, X.B., 2014. Metallogeny in response to lithospheric thinning and craton destruction: geochemistry and U-Pb zircon chronology of the Yixingzhai gold deposit, central North China Craton. Ore Geol. Rev. 56, 457–471.
Li, S.R., Santosh, M., Zhang, H.F., 2013. Inhomogeneous lithospheric thinning in the central North China Craton: zircon U-Pb and S-He-Ar isotopic record from magmatism and metallogeny in the Taihang Mountains. Gondwana Res. 23, 141–160.
Li, Y., Geng, Z.Q., 1997. Gold metallogenic regularity and exploration direction in middle sector of north margin of North China platform. Gold Geol. 1, 23–30 (in Chinese with English abstract).
Li, Y.G., Wang, L., 2002. The study on wall rock alteration of Niujuan silver (gold) deposit, Hebei province, China. Contrib. Geol. Miner. Resour. Res. 17, 234–239 (in Chinese with English abstract).
Li, Z.Y., Liu, X.Y., Li, S.M., Hu, H.B., Yang, Y., 2014. An analysis of geological age and materials source of the Niujuan Ag-Au polymetallic deposit in Chengde. Geol. China 41, 951–960 (in Chinese with English abstract).
Liu, C., Nie, F., Bagas, L., 2016. Geology and ore genesis of the Yu'erya gold deposit, eastern Hebei Province, China. Ore Geol. Rev. 73, 270–283.
Liu, C.H., Liu, J.J., Carranza, E.J.M., Yang, L.B., Wang, J.P., Zhai, D.G., Wang, Y.H., Wu, J., Dai, H.Z., 2015. Geological and geochemical constraints on the genesis of the Huachanggou gold deposit, western Qinling region, central China. Ore Geol. Rev. 73, 354–373.
Liu, F.S., Zhang, G.H., 1997. Genesis and prospecting criteria of Niujuan hot spring type Ag(Au) deposit in Fengning County, Hebei Province. J. Geol. Miner. Resour. North China 12, 137–146 (in Chinese with English abstract).
Liu, J.M., Zhao, S.R., Shen, J., Jiang, N., Huo, W.G., 1998. Review on direct isotopic dating of hydrothermal oreforming processes. Adv. Geophys. 13 46-45 (in Chinese with English abstract).
Long, K.R., DeYoung, J.H., Ludington, S.D., 1998. Database of significant deposits of gold, silver, copper, lead, and zinc in the United States; Part A: Database description and analysis. US Geological Survey Open-File Report.
Ludwig, K.R., 2003. User's manual for Isoplot/EX Version 3.00. A geochronological toolkit for Microsoft Excel. Berkeley Geochronol. Centre, Spec. Publ. 4, 1–71.
Mango, H., Zantop, H., Oreskes, N., 1991. A fluid inclusion and isotope study of the Rayas Ag-Au-Cu-Pb-Zn mine, Guanajuato, Mexico. Econ. Geol. 86, 1554–1561.
McPhie, J., Kamenetsky, V., Allen, S., Ehrig, K., Agangi, A., Bath, A., 2011. The fluorine link between a supergiant ore deposit and a silicic large igneous province. Geology 39, 1003–1006.
Meng, E., Xu, W.L., Yang, D.B., Qiu, K.F., Li, C.H., Zhu, H.T., 2011. Zircon U-Pb chronology, geochemistry of Mesozoic volcanic rocks from the Lingquan basin in Manzhouli area, and its tectonic implications. Acta Petrol. Sinica 27, 1209–1226 (in Chinese with English abstract).
Meng, Q.R., 2003. What drove late Mesozoic extension of the northern China-Mongolia tract? Tectonophysics 369, 155–174.
Musgrave, J.A., Thompson, T.B., 1991. Sultan Mountain Mine, western San Juan Mountains, Colorado; a fluid inclusion and stable isotope study. Econ. Geol. 86, 768–779.
Nie, F.J., Zhang, W.Y., Jiang, S.H., 2007a. Discussion on the time limitation of silver (gold) mineralization in the Niujuan deposit, Northern Hebei province. Earth Sci. Front. 7, 35–51 (in Chinese with English abstract).
Nie, F.J., Zhang, W.Y., Jiang, S.H., Liu, Y., 2007b. Discussion on the time limitation of silver (gold) mineralization in the Niujuan deposit, Northern Hebei Province. Earth Sci. Front. 14, 167–176 (in Chinese with English abstract).
Ohmoto, H., 1972. Systematics of sulfur and carbon isotopes in hydrothermal ore deposits. Econ. Geol. 67, 551–578.
Ohmoto, H., Rye, R.O., 1979. Isotopes of sulfur and carbon. In: Barnes, H.L. (Ed.), Geochemistry of Hydrothermal Ore Deposits. Wiley, New York, pp. 509–567.
Ouyang, H.G., Mao, J.W., Santosh, M., Zhou, J., Zhou, Z.H., Wu, Y., Hou, L., 2013. Geodynamic setting of Mesozoic magmatism in NE China and surrounding regions: perspectives from spatio-temporal distribution patterns of ore deposits. J. Asian Earth Sci. 78, 222–236.
Pei, J.L., Sun, Z.M., Liu, J., Liu, J., Wang, X.S., Yang, Z.Y., Zhao, Y., Li, H.B., 2011. A paleomagnetic study from the Late Jurassic volcanics (155 Ma), North China: implications for the width of Mongol-Okhotsk Ocean. Tectonophysics 510, 370–380.
Peng, J., Yazhou, F.U., Yuan, S., Shen, N., 2006. Sm-Nd isotope dating of some ca-bearing minerals in hydrothermal deposits. Geol. Rev. 52, 662–667.
Pirajno, F., 2009. Hydrothermal Processes and Mineral Systems, Springer, 1–1250.
Sakai, H., 1968. Isotopic properties of sulfur compounds in hydrothermal processes. Geochem. J. 2, 29–49.
Santosh, M., 2010. Assembling North China Craton within the Columbia supercontinent: the role of double-sided subduction. Precambr. Res. 178 (1), 149–167.
Santosh, M., Teng, X.M., He, X.F., Tang, L., Yang, Q.Y., 2016. Discovery of Neoarchean suprasubduction zone ophiolite suite from Yishui Complex in the North China Craton. Gondwana Res. 38, 1–27.
Santosh, M., Zhao, D.P., Kusky, T.M., 2010. Mantle dynamics of the Paleoproterozoic North China Craton: a perspective based on seismic tomography. J. Geodyn. 49, 39–53.
Saravanan, C.S., Mishra, B., 2009. Uniformity in sulfur isotope composition in the orogenic gold deposits from the Dharwar Craton, southern India. Miner. Deposita 44, 597–605.
Seward, T.M., Barnes, H.L., 1997. Metal transport by hydrothermal ore fluids. In: Barnes, H.L. (Ed.), Geochemistry of Hydrothermal Ore Deposits. John Wiley and Sons, New York, pp. 435–486.
Shen, L.X., Li, W.S., Wang, Z.L., Ma, J.X., Li, C.Y., 2012. Forecast for the deep mineralization of Niujuan silver-gold deposit and Yingfang silver-lead-zinc deposit in northern Hebei province. Contrib. Geol. Miner. Resour. Res. 4, 450–457 (in Chinese with English abstract).
Sibson, R.H., 1994. Crustal stress, faulting and fluid flow. In: Parnell, J. (Ed.), Geological Society Special Publications 78, 69–84.
Smith, D.M., Albinson, T., Sawkins, F.J., 1982. Geologic and fluid inclusion studies of the Tayoltita silver-gold vein deposit, Durango, Mexico. Econ. Geol. 77, 1120–1145.
Song, R.X., 1994. Hebei Gold Deposit Geology. Geological Publishing House, Beijing, pp. 194–200.
Song, M.C., Li, S.Z., Santoshd, M., Zhao, S.J., Yu, S., Yi, P.H., Cui, S.X., Lv, G.X., Xu, J.X., Song, Y.X., Zhou, M.L., 2015. Types, characteristics and metallogenesis of gold deposits in the Jiaodong Peninsula, Eastern North China Craton. Ore Geol. Rev. 65, 612–625.
Stuart, F.M., Burnard, P.G., Taylor, R.P., Turner, G., 1995. Resolving mantle and crustal contributions to ancient hydrothermal fluids: He-Ar isotopes in fluid inclusions from Dae Hwa W-Mo mineralisation, South Korea. Geochim. Cosmochim. Acta: J. Geochem. Soc. Meteoritical Soc. 59, 4663–4673.
Sun, J.G., Han, S.J., Zhang, Y., Xing, S.W., Bai, L.A., 2012. Diagenesis and metallogenetic mechanisms of the Tuanjiegou gold deposit from the Lesser Xing'an Range, NE China: zircon U-Pb geochronology and Lu–Hf isotopic constraints. J. Asian Earth Sci. 62, 373–388.
Sun, S.L., Chen, J.F., Zhen, J.J., Liu, W.H., 2009. The noble gas isotope geochemical composition of chert at the bottom of Cambrian in Tarim Basin, China. Sci. China Ser. D-Earth Sci. 52, 115–119.
Sun, X., Deng, J., Zhao, Z.Y., Wang, Q.F., Yang, L.Q., Gong, Q.J., Wang, C.M., 2010.

Geochronology, petrogenesis and tectonic implications of granites from the Fuxin area, Western Liaoning, NE China. Gondwana Res. 17, 642–652.
Taylor, H.P., 1974. The application of oxygen and hydrogen isotope studies to problems of hydrothermal alteration and ore deposition. Econ. Geol. 69, 843–883.
Tolstikhin, I.N., 1978. A review: some recent advances in isotope geochemistry of light rare gases. In: Alexander, E.C., Ozima, M. (Eds.), Terrestrial Rare Gases. Japan Scientific Society Press, Tokyo, pp. 27–62.
Wang, B.D., Niu, S.Y., Li, H.Y., Sun, A.Q., Wu, X.G., 2005. Mantle branch structure and mineralization controls on Au-Ag and polymetallic ore deposits in the northern Hebei province. Geol. Prospect. 41, 7–12 (in Chinese with English abstract).
Wang, F., Zhou, X.H., Zhang, L.C., Ying, J.F., Zhang, Y.T., Wu, F.Y., Zhu, R.X., 2006. Late Mesozoic volcanism in the Great Xing'an Range (NE China): timing and implications for the dynamic setting of NE Asia. Earth Planet. Sci. Lett. 251, 179–198.
Wang, T., Guo, L., Zheng, Y.D., Donskaya, T., Gladkochub, D., Zeng, L.S., Li, J.B., Wang, Y.B., Mazukabzov, A., 2012. Timing and processes of late Mesozoic mid-lower crustal extension in continental NE Asia and implications for the tectonic setting of the destruction of the North China Craton: mainly constrained by zircon U-Pb ages from metamorphic core complexes. Lithos 154, 315–345.
Wang, Y.X., Yang, J.D., Chen, J., 2007a. The Sr and Nd isotopic variations of the Chinese Loess Plateau during the past 7 Ma: implications for the East Asian winter monsoon and source areas of loess. Palaeogeogr. Palaeoclimatol. Palaeoecol. 249, 351–361.
Wang, Y.X., Yang, J.D., Chen, J., Zhang, K.J., Rao, W.B., 2007b. The Sr and Nd isotopic variations of the Chinese Loess Plateau during the past 7 Ma: implications for the East Asian winter monsoon and source areas of loess. Palaeogeogr. Palaeoclimatol. Palaeoecol. 249, 351–361.
Winckler, G., Aeschbach-Hertig, W., Kipfer, R., Reiner Botz, R., Rübel, A.P., Bayer, R., Stoffers, P., 2001. Constraints on origin and evolution of Red Sea brines from helium and argon isotopes. Earth Planet. Sci. Lett. 184, 6.
Wood, S., Samson, I., 1998. Solubility of ore minerals and complexation of ore metals in hydrothermal solutions. Rev. Econ. Geol. 10, 33–80.
Wu, F.Y., Jahn, B.M., Wilde, S.A., Lo, C.H., Yui, T.F., Lin, Q., Ge, W.C., Sun, D.Y., 2003. Highly fractionated I-type granites in NE China (I): geochronology and petrogenesis. Lithos 66, 241–273.
Wu, F.Y., Li, X.H., Yang, J.H., Zheng, Y.F., 2007. Discussions on the petrogenesis of granites. Acta Petrol. Sinica 23, 1217–1238.
Wu, F.Y., Lin, J.Q., Wilde, S.A., Zhang, X.O., Yang, J.H., 2005. Nature and significance of the Early Cretaceous giant igneous event in eastern China. Earth Planet. Sci. Lett. 233, 103–119.
Xu, G., Xu, S.Z., Zhang, Y.H., 1995. Geologic features and prospecting guidelines for gold deposits in northern Hebei. Gold Geol. 1, 13–18 (in Chinese with English Abstract).
Xu, W.G., Fan, H.R., Hu, F.F., Santosh, M., Yang, K.F., Lan, T.G., et al., 2015. Geochronology of the Guilaizhuang gold deposit, Luxi block, eastern North China Craton: constraints from zircon U-Pb and fluorite-calcite Sm-Nd dating. Ore Geol. Rev. 65, 390–399.
Xu, W.L., Pei, F.P., Gao, F.H., Yang, D.B., Bu, Y.J., 2008. Zircon U-Pb age from basement granites in Yishu granben and its tectonic implications. Earth Sci. 33, 145–150.
Xu, W.L., Wang, F., Pei, F.P., Meng, E., Tang, J., Xu, M.J., Wang, W., 2013. Mesozoic tectonic regimes and regional ore-forming background in NE China: constraints from spatial and temporal variations of Mesozoic volcanic rock associations. Acta Petrol. Sinica 29 (2), 339–353.
Xu, W.L., Wang, Q.H., Wang, D.Y., Pei, F.P., Gao, S., 2004. Processes and mechanism of Mesozoic lithospheric thinning in eastern North China Craton: evidence from Mesozoic igneous rocks and deep-seated xenoliths. Earth Sci. Front. 11, 309–317 (in Chinese with English Abstract).
Yamamoto, J., Nishimura, K., Sugimoto, T., Takemura, K., Takahata, N., Sano, Y., 2009. Diffusive fraction of noble gases in mantle with magma channels: origin of low He/Ar in mantle-derived rocks. Earth Planet. Sci. Lett. 280, 167–174.
Yang, J., Lv, G.Z., 2006. The gold mineralization condition and ore-prospecting sign in fengning-Chengde area, Hebei. Gold Sci. Technol. 2, 52–56 (in Chinese with English Abstract).
Yang, Q.Y., Santosh, M., 2017. The building of an Archean microcontinent: evidence from the North China Craton. Gondwana Res. 50, 3–37.
Yang, Q.Y., Santosh, M., Collins, A.S., Teng, X.M., 2016. Microblock amalgamation in the North China Craton: evidence from Neoarchaean magmatic suite in the western margin of the Jiaoliao Block. Gondwana Res. 31, 96–123.
Yang, Q.Y., Santosh, M., 2015a. Paleoproterozoic arc magmatism in the North China Craton: no Siderian global plate tectonic shutdown. Gondwana Res. 28, 82–105.
Yang, Q.Y., Santosh, M., 2015b. Early Cretaceous magma flare-up and its implications on gold mineralization in the Jiaodong Peninsula, China. Ore Geol. Rev. 65, 626–642.
Yang, S.D., 2000. Ore forming geological characteristics and scientific prospecting for silver deposits in north Hebei province [Master's dissertation]. Guangzhou, Central South University of Technology, p. 7 (in Chinese with English abstract).
Ye, X.R., Tao, M.X., Yu, C.A., Zhang, M.J., 2007. Helium and neon isotopic compositions in the ophiolites from the Yarlung Zangbo River, Southwestern China: the information from deep mantle. Sci. China (Ser. D) 50, 801–812.
Yuan, H.L., Gao, S., Liu, X.M., Li, H.M., Gunther, D., Wu, F.Y., 2004. Accurate U-Pb age and trace element determination of zircon by laser ablation-inductively coupled plasma-mass spectrometry. Geostand. Geoanal. Res. 28, 353–370.
Zartman, R.E., Doe, B.R., 1981. Plumbotectonic – the model. Tectonophysics 75, 135–162.
Zhai, M.G., Santosh, M., 2011. The early Precambrian odyssey of the North China Craton: a synoptic overview. Gondwana Res. 20, 6–25.
Zhai, M.G., 2004. 2.1 ~ 1.7 Ga geological event group and its geotectonic significance. Acta Petrol. Sinica 20, 1343–1354 (in Chinese with English Abstract).
Zhai, M.G., 2010. Tectonic evolution and metallogenesis of North China Craton. Mineral Deposits 29, 24–36 (in Chinese with English Abstract).
Zhang, H.F., Zhu, R.X., Santosh, M., Ying, J.F., Su, B.X., Hu, Y., 2013. Episodic widespread magma underplating beneath the North China Craton in the Phanerozoic: implications for craton destruction. Gondwana Res. 23, 95–107.
Zhang, J.H., Gao, S., Ge, W.C., Wu, F.Y., Yang, J.H., Wilde, S.A., Li, M., 2010. Geochronology of the Mesozoic volcanic rocks in the Great Xing'an Range, northeastern China: implications for subduction-induced delamination. Chem. Geol. 276, 144–165.
Zhang, W.X., Zhao, G.R., 2009. Analysis on the metallogenic condition of gold in Yanshan region. Gold Sci. Technol. 17, 28–33 (in Chinese with English abstract).
Zhao, G.C., Cawood, P.A., Wilde, S.A., Sun, M., Lu, L.Z., 2000. Metamorphism of basement rocks in the Central Zone of the North China Craton: implications for Paleoproterozoic tectonic evolution. Precambrian Res. 103, 55–88.
Zhao, G.C., Zhai, M.G., 2013. Lithotectonic elements of Precambrian basement in the North China Craton: review and tectonic implications. Gondwana Res. 23 (4), 1207–1240.
Zhao, Z., Zhang, P., Xiong, X., Wang, Q., 2005. Au-Te deposits associated with alkali-rich igneous rocks in China. In: Mao, J., Bierlein, F.P. (Eds.), Mineral Deposit Research: Meeting the Global Challenge. Springer, Berlin Heidelberg, pp. 1451–1454.
Zhao, Z.F., 1993. The Evolution of the Precambrian Crust in the Sino – Korean Quasi – Platform. Science Press (in Chinese).
Zheng, Y.F., Chen, J.F., 2000. Geochemistry of Stable Isotopes. Science Press, Beijing, pp. 1–316 (in Chinese).
Zhu, B.Q., 1998. The Theory and Application of the Isotopic Systematic in Geoscience-Concurrent Discussion of the Continental Crust and Mantle Evolvement in China. Science Publishing House, Beijing, pp. 1–330 (in Chinese with English abstract).
Zhu, R., Xu, Y., Zhu, G., Zhang, H., Xia, Q., Zheng, T., 2012. Destruction of the north China Craton. Sci. China Earth Sci. 55, 1565–1587.
Zhu, R.X., Chen, L., Wu, F.Y., Liu, J.L., 2011. Timing, scale and mechanism of the destruction of the North China Craton. Sci. China Earth Sci. 54, 789–797.